

Galaxy populations in groups and clusters: evidence for a characteristic stellar mass scale at $M_* \sim 10^{9.5} M_\odot$

JIACHENG MENG ¹, CHENG LI ¹, H.J. MO ², YANGYAO CHEN ³, ZHEN JIANG ¹ AND LIZHI XIE ^{4,5}

¹*Department of Astronomy, Tsinghua University, Beijing 100084, China*

²*Department of Astronomy, University of Massachusetts Amherst, MA 01003, USA*

³*Department of Astronomy, University of Science and Technology of China, Hefei Anhui 230026, China*

⁴*Tianjin Normal University, Binshuixidao 393, 300387, Tianjin, China*

⁵*INAF - Astronomical Observatory of Trieste, via G.B. Tiepolo 11, I- 34143 Trieste, Italy*

ABSTRACT

We use the most recent data release (DR9) of the DESI legacy imaging survey and SDSS galaxy groups to measure the conditional luminosity function (CLF) for groups with halo mass $M_h \geq 10^{12} M_\odot$ and redshift $0.01 \leq z \leq 0.08$, down to a limiting r -band magnitude of $M_r = -10 \sim -12$. For a given halo mass we measure the CLF for the total satellite population, as well as separately for the red and blue populations classified using the $(g - z)$ color. We find a clear faint-end upturn in the CLF of red satellites, with a slope $\alpha \approx -1.8$ which is almost independent of halo mass. This faint-end upturn is not seen for blue satellites and for the total population. Our stellar population synthesis modeling shows that the $(g - z)$ color provides a clean red/blue division, and that group galaxies in the red population defined by $(g - z)$ are all dominated by old stellar populations. The fraction of old galaxies as a function of galaxy luminosity shows a minimum at a luminosity $M_r \sim -18$, corresponding to a stellar mass $M_* \sim 10^{9.5} M_\odot$. This mass scale is independent of halo mass and is comparable to the characteristic luminosity at which galaxies show a dichotomy in surface brightness and size, suggesting that the dichotomy in the old fraction and in galaxy structure may have a common origin. The rising of the old fraction at the faint end for Milky Way (MW)-sized halos found here is in good agreement with the quenched fraction measured both for the MW/M31 system and from the ELVES survey. We discuss the implications of our results for the formation and evolution of low-mass galaxies, and for the stellar mass functions of low-mass galaxies to be observed at high redshift.

Keywords: Galaxy clusters(584) — Galaxy groups(597) — Galaxy abundances(574) — Galaxy formation(595)

1. INTRODUCTION

In the current paradigm of structure and galaxy formation, galaxies form in dark matter halos through a two-stage process, in which dark halos form in the first place by gravitational instability of initial density perturbations, followed by the formation of galaxies at the centers of dark halos through gas cooling and condensation (White & Rees 1978; Mo et al. 2010, and references therein). Halos grow in dark matter mass by both mass

accretion and halo-halo mergers. A galaxy at the center of its host halo, called the central galaxy, grows its stellar mass by forming stars from the cooled gas and by accreting stars that have formed elsewhere. At a later time, a halo may fall into a bigger halo and become a subhalo, and the central galaxy hosted by it then becomes a satellite galaxy in the new host. As a satellite, it is affected by environmental effects in the host halo, such as tidal stripping and ram-pressure stripping, which may effectively reduce the hot and even cold gas contents of the galaxy, shutting down its star formation and making it quenched and red. On the other hand, physical processes internal to the galaxy, such as energy feedback from supernovae and active galactic nuclei may be able to heat and/or eject the cold gas, which may also quench

Corresponding author: Jiacheng Meng & Cheng Li
mengjc18@mails.tsinghua.edu.cn

cli2015@tsinghua.edu.cn

the star formation and make the galaxy red. Thus, the formation and evolution of galaxies are expected to be driven by a variety of factors, including the assembly history and properties of (sub)halos of galaxies and internal processes and properties of galaxies. In order to obtain a full understanding of galaxy formation and evolution, therefore, it is crucial to establish a statistical link of the properties of galaxies to their dark matter (sub)halos.

To this end, large amounts of effort have been devoted to measuring the luminosity function (LF) and stellar mass function (SMF) of galaxies in clusters and groups of galaxies, so as to quantify the galaxy population in halos of different mass and in systems of different richness. Early studies were usually limited to nearby rich clusters, and the LFs of cluster galaxies were found to be roughly consistent with a Schechter form in the bright end, but with some sign of a steepening in the faint-end (e.g. Binggeli et al. 1988; Driver et al. 1994; Bernstein et al. 1995; de Propris et al. 1995; Yagi et al. 2002; Parolin et al. 2003; Popesso et al. 2005, 2006; Barkhouse et al. 2007, 2009). This faint-end upturn was also found in galaxy groups in the local Universe (e.g. Zandivarez et al. 2006; Yang et al. 2009; Robotham et al. 2010; Zandivarez & Martínez 2011), mainly from the spectroscopic galaxy sample of the Sloan Digital Sky Survey (SDSS; York et al. 2000). However, these findings of a significant faint-end upturn were questioned by other investigations using data from, e.g., the SDSS (Hansen et al. 2009; de Filippis et al. 2011) and the HST (Harrison & De Propris 2009). Results obtained for individual systems in the nearby Universe also show significant variance (see Boselli & Gavazzi 2014, for a review), with a significant faint-end upturn present for some clusters, such as A1689 (Bañados et al. 2010), Coma (Mobasher et al. 2003; Yamanoi et al. 2012) and Abell 119 (Lee et al. 2016)), but absent for some others, such as Virgo (Rines & Geller 2008; Lieder et al. 2012; Ferrarese et al. 2016), Hydra (Yamanoi et al. 2007; Misgeld et al. 2008, 2009) and Abell 85 (Agulli et al. 2014). More recently, Hashimoto et al. (2022) measured the LFs of dwarf galaxies in 33 galaxy clusters at $z \sim 0.15 - 0.3$ using data obtained from the Subaru Superime-Cam imaging survey, and found that the faint-end slope is rather flat, with $\alpha = -1.2 \sim -1.4$. In contrast, analyses using central galaxies and groups selected from the SDSS spectroscopic data in combination with satellite galaxies sampled by photometric data from SDSS (Lan et al. 2016), from DESI (Tinker et al. 2021) and from a combination of SDSS, DESI and HSC (Wang et al. 2021) revealed that the faint end of the conditional luminosity function (CLF) of galaxies shows a significant upturn for halos of

all mass, and the upturn is particularly strong for red satellites, with $\alpha \approx -1.8$ (Lan et al. 2016).

These measurements provide important information about the galaxy-halo connection and on the physical processes behind it (e.g. see Wechsler & Tinker 2018 for a review). In particular, the faint-end slope of the LFs in groups/clusters provides a unique way to understand the formation and evolution of low-mass galaxies. For instance, in the empirical model developed by Lu et al. (2014) and Lu et al. (2015), a high efficiency of star formation at $z > 2$ is required for their model to reproduce the faint-end upturn in the cluster galaxy LF obtained by Popesso et al. (2006). In Lan et al. (2016), the subhalo abundance matching method was used to relate the faint-end slope (α) of the CLFs of the SDSS galaxy groups to the power-law slope (β) of the galaxy luminosity-subhalo mass relation ($L \propto m^\beta$). They obtained $L \propto m$ for low-mass red satellites in comparison to $L \propto m^{3/2}$ for their blue counterparts. The relation $L \propto m$ indicates that low-mass red satellites formed their stars with an efficiency independent of halo mass, a result that has important implications for star formation and feedback in these systems. The observed results are consistent with the empirical model of Lu et al. (2014) and Lu et al. (2015) and the pre-heating model of Mo & Mao (2002) and Mo & Mao (2004), both predicting enhanced star formation efficiency in low-mass halos at high redshift. Clearly, reliable observational results are required to test these predictions. In addition, the satellite population in clusters of galaxies may also be related to the origin of the chemical enrichment of the intracluster medium (ICM). Trentham (1994) suggested that the precursors of dwarf galaxies, in which supernova-driven winds may expel gas effectively, can account for the enrichment of the ICM if the faint-end slope is steep, $\alpha \sim -1.9$. However, Gibson & Matteucci (1997) showed that the precursors of the dwarf galaxies cannot account for the chemical content of the ICM even if the faint-end slope is steep. Thus, the importance of the satellite population for the enrichment of the ICM is still uncertain.

In this paper, we attempt to obtain reliable measurements of the CLF down to unprecedented limits for galaxy groups in the local Universe. The CLF was originally proposed by Yang et al. (2003) and has been studied extensively using both spectroscopic and photometric samples (e.g. van den Bosch et al. 2003; Hansen et al. 2005; Cooray 2006; van den Bosch et al. 2007; Hansen et al. 2009; Yang et al. 2009; Guo et al. 2011a; Wang & White 2012; Sales et al. 2013; Lan et al. 2016; Guo et al. 2018; Vázquez-Mata et al. 2020; Tinker et al. 2021; Wang et al. 2021). We use central galaxies iden-

tified by applying the halo-based group finder of Yang et al. (2005) to the galaxy sample of SDSS data release 7 (Yang et al. 2007). CLFs have also been measured for SDSS groups by Lan et al. (2016, hereafter L16) using the SDSS photometric sample to trace the satellite population, and by Tinker et al. (2021) using an earlier data release of the DESI imaging survey. Here, we use the most recent imaging data from the DESI legacy survey (DESI-DR9; Dey et al. 2019), which is deeper and provides better photometry than data used in previous studies. In addition, we will use the $(g-z)$ color instead of the commonly-used $(u-r)$ color to separate galaxies into red and blue populations. As we will show, the $(u-r)$ is sensitive to young stellar populations, and it may mis-classify “old” galaxies dominated by old stellar populations as blue galaxies due to the contamination of a small fraction of young populations, particularly for low-mass galaxies of low metallicity. The $(g-z)$ provides a cleaner color division, which allows us to measure the CLFs of faint galaxies more reliably for both the old and young satellite populations. Our analysis leads to the finding of a characteristic mass scale at $M_* \sim 10^{9.5} M_\odot$ in the relation between the old fraction and the stellar mass, and that the mass scale is quite independent of halo mass. This indicates a dichotomy of the satellite population in quenching processes.

The paper is organized as followed. In section 2 we describe the imaging data and the group catalogue used in our analyses. section 3 presents our measurements of the conditional luminosity functions. In section 4 we study the old satellite population versus their young counterpart, and use stellar population synthesis models to explore the origin of the color bimodality observed for galaxies in groups. We discuss our results in section 5 and summarize them in section 6. Throughout the paper, we assume a Λ CDM cosmology with $\Omega_m = 0.275$ and $H_0 = 70.2 \text{ km s}^{-1} \text{ Mpc}^{-1}$ following the WMAP7 results (Komatsu et al. 2011). We define the mass and radius of a dark matter halo so that the mean mass density within the radius is 200 times the mean density of the universe. For convenience, we use M_h and r_h , instead of M_{200m} and r_{200m} , to denote these quantities.

2. DATA

2.1. SDSS galaxies and groups

We use galaxy groups identified by Yang et al. (2007) from the NYU value-added galaxy catalogue Blanton et al. (NYU-VAGC; 2005b), a catalog of low- z galaxies based on SDSS data release 7 (DR7; Abazajian et al. 2009). These groups were selected using the halo-based group finder of Yang et al. (2005), which uses an iterative method adapted to the properties of dark matter

halos. Unlike the Friend-of-Friend (FoF) method, the halo-based finder is capable of identifying poor groups, even those with only one member. We use the group catalogue constructed from galaxy Sample II, which covers an area of 7748 deg^2 and contains galaxies from the SDSS main sample with redshift $0.01 \leq z \leq 0.2$ and with redshift completeness $\mathcal{C} > 0.7$. Sample II also includes 7091 galaxies with redshift from other surveys, such as the 2dFGRS (Colless et al. 2001), but it does not include galaxies missing redshift measurements due to fiber collision. Yang et al. (2007) used two methods to assign halo mass to galaxy groups, based on the ranks of either the total stellar mass or the total r -band luminosity of all group members with $M_r - 5 \log h \leq 19.5$. Here we use halo masses, M_h , estimated from the total stellar mass. The halo sample with $M_h \geq 10^{12} M_\odot$ are complete at $z \leq 0.08$. We thus use the group/halo sample with $0.01 \leq z \leq 0.08$ and $M_h \leq 10^{12} M_\odot$ for our analyses, unless otherwise stated.

In our analyses, we also use both spectroscopic and photometric galaxies from the SDSS. Spectroscopic galaxies are used to estimate K -corrections for photometric galaxies and to check results obtained from photometric samples. The spectroscopic galaxies used are also from NYU-VAGC, and K -corrections of galaxies are obtained using `kcorrect v4.1.4` (Blanton & Roweis 2007). As we will describe below, the DESI imaging data, which we will also use for our analyses, provides only photometry in the g , r and z bands. We will supplement the data with the u -band photometry from the SDSS when needed. The SDSS photometric galaxies are selected from the SDSS data release 16 (DR16; Ahumada et al. 2020). We use galaxies with r -band model magnitudes $r < 21$ to guarantee completeness of the data. We note that SDSS photometry is used only for the u -band; magnitudes in all other bands are from the DESI image data.

We use two methods to do the K -correction for photometric galaxies, both based on the K -correction values of the SDSS main sample provided in the NYU-VAGC. In the first method, we create a grid in observed $(g-r)$ color versus $(r-z)$ color space to obtain the median K -correction in each band as a function of redshift for each of the color-color bins. The value of the K -correction for each photometric galaxy in a color-color bin is then estimated using the redshift of the galaxy group to which the galaxy is assigned. The second method is to use the nearest galaxies in the SDSS spectroscopic sample. For each photometric galaxy, we find its nearest neighbor, in the spectroscopic sample, which is closest to it in the observed $(g-r)$ - $(r-z)$ -redshift space, and use the K -correction value of the nearest spectroscopic neigh-

bor as its K -correction. Here the ‘distance’ (which decides the nearest neighbor of a galaxy) is defined as the square root of $\Delta^2(g-r) + \Delta^2(r-z) + \Delta^2z$. The redshift used for the photometric galaxies are the redshift of the galaxy group. We find that the two methods give very similar results, and our following presentation is based on the second method.

2.2. The DESI imaging data

The DESI legacy imaging survey (DESI-DR9, Dey et al. 2019) consists of three parts: the Beijing-Arizona Sky Survey (BASS), Mayall z -band Legacy Survey (MzLS), and DECam Legacy Survey (DECaLS). The depths at 5σ are about $g = 24.7$, $r = 23.9$, and $z = 23.0$, respectively, and the total sky coverage is about $14,000\text{deg}^2$. We use galaxies that have $r < 23$ and meet the following selection criteria:

1. TYPE = “REX”, “EXP”, “DEV” or “SER”;
2. FRACFLUX_R < 2;
3. FRACMASKED_R < 0.6.

Here TYPE represents the morphological type of the sources, and the four types listed above are considered as galaxies. FRACFLUX_R represents the profile-weighted fraction of the r -band flux of a source that comes from other sources. We have tested using other criteria, such as $\text{FRACFLUX_R} < 2.5$ or 3, and found no significant impact on our results. FRACMASKED_R represents the fraction of masked pixels of an object in the r -band, and here we follow the criterion used in Tinker et al. (2021). We find that some sources listed in the catalogue are substructures of bigger galaxies. We use the following method to remove them. For each galaxy in DESI-DR9, we use its half light radius, SHAPE_R, and its orientation and axis ratio specified by SHAPE_E1 and SHAPE_E2 to determine an ellipse with a linear size twice as large as that given by the half-light radius. We exclude all galaxies that reside in the ellipse of another galaxy. The factor of two in the linear size of the ellipse is chosen somewhat arbitrarily, but our tests using other factors show that our results are not sensitive to the choice. DESI-DR9 also provides random samples of the survey and we use them to model the survey mask.

For some of our analyses, we also need the u -band photometry, which is not provided by DESI-DR9. As a remedy, we use the u -band photometry from SDSS to supplement the data. Galaxies are cross-matched using centroid positions, (RA, Dec), provided by the two catalogs. Because the SDSS survey is shallower than DESI-DR9, we only match galaxies with $r < 21$ to guarantee the completeness of the SDSS data. Thus, only galaxies

with $r < 21$ are used in the analyses that involve the u -band data.

Since no redshift is available for photometric galaxies, K -corrections cannot be applied directly for them. As mentioned above, we use the K -corrections obtained from the spectroscopic sample and matching in color-color space to estimate the K -corrections of photometric galaxies. There are some systematic offsets between the SDSS and DESI magnitudes. To account for these offsets, we first match SDSS spectroscopic galaxies to the DESI image data to get their DESI-DR9 g , r and z magnitudes, and assume that galaxies at the same position in $(g-r)$ - $(r-z)$ -redshift space have a similar K -correction. For each photometric galaxy, which is determined to be associated to a given group (see below), we then identify its nearest spectroscopic galaxy in $(g-r)$ - $(r-z)$ -redshift space, where the redshift of the photometric galaxy is that of the group. Finally, we use the K -correction of the spectroscopic galaxy as the K -correction for the photometric galaxy in question.

3. GALAXIES IN HALOS OF GALAXY GROUPS

3.1. Method to identify member galaxies

Because there is no spectroscopic redshift for photometric galaxies, it is difficult to identify member galaxies in a galaxy group in a deterministic way. Here we use the same method as used in L16 to identify member galaxies statistically. Our goal is to obtain the distribution of member galaxies in the space spanned by galaxy properties, represented collectively by \vec{q} , in groups of given halo mass, i.e. the conditional distribution function, $\Phi(\vec{q} | M_h)$. To this end, we cross-correlate galaxy groups with photometric galaxies. Since galaxy groups are identified from the spectroscopic data, their redshifts are known. For the i -th group with redshift z_i , we identify all photometric galaxies within the angular radius of the group (obtained from its physical radius and redshift), and assign the redshift z_i to all of them. The redshift is then used to calculate physical quantities of the photometric galaxy, such as absolute magnitudes and rest-frame colors. Finally, we obtain the conditional function, $\Phi_{\text{grp},i}(\vec{q} | M_h)$, of the property \vec{q} of interest for group i from the corresponding observational quantity and z_i . Since we count all galaxies within the projected halo radius r_h , the distribution function obtained above contains galaxies that are not true members, but foreground/background galaxies that are selected because of projection. For brevity, we will refer to these foreground/background galaxies collectively as background galaxies. To subtract the contribution of the background galaxies, we use an annulus with inner and outer radii of $2.5r_h$ and $3r_h$ around the group in question, and identify

all photometric galaxies, all assumed to be at z_i , within the annulus. Here again, we use the group redshift, z_i to estimate \vec{q} from observational quantities. The corresponding galaxy distribution, $\Phi_{\text{bkg},i}(\vec{q} | M_h)$, can then be estimated. Averaging over all groups with similar halo mass, we get the conditional distribution function, with the background subtracted:

$$\Phi(\vec{q} | M_h) = \langle \Phi_{\text{grp},i}(\vec{q} | M_h) - f_{A,i} \times \Phi_{\text{bkg},i}(\vec{q} | M_h) \rangle_i, \quad (1)$$

where $f_{A,i}$ is the area ratio between the group and the annulus.

L16 used two methods to estimate the background contribution. The first is a local estimator, which uses galaxies in annulus around individual groups, as described above. The second one is a global estimator, which uses the average of the galaxy counts in eight randomly selected circles, each with a radius corresponding to the halo radius r_h , to estimate the background for the galaxy group in question. We have made tests using the two methods and found that the local estimator performs better. The global estimator ignores background fluctuations from place to place, leading to an underestimate of the conditional distribution functions. Because of this, we adopt the local estimator for our analyses.

In our analysis, we use 200 bootstrap re-samplings of groups to estimate measurement errors. Previous investigations have shown that clustering of background galaxies may affect error estimates (Huang et al. 1997; Driver et al. 2003; Pracy et al. 2004). Driver et al. (2003) proposed a formula to model the effects of clustering of background galaxies. In our analysis, an annulus outside the group region is used as the reference region for background subtraction. Thus, for each cluster/group of an angular size, the number count within its aperture consists of two parts: that of its member galaxies, N_C , and that of background galaxies N_B , with the latter estimated from the count of galaxies in the annulus, N_A . To estimate the impact of clustering on our background subtraction, we first randomly select positions across the DESI sky coverage. We then obtain the number counts of galaxies, N_B , within an aperture of radius θ around these positions, and the corresponding counts, N_A , in the annulus between 2.5θ and 3θ . We estimate the average and variance of $(N_B - f_A N_A)$ as functions of both θ and the apparent magnitude m_r . We find that the averages are all around 0, suggesting that our method to subtract the background is unbiased. As a test, we include the variance of $(N_B - f_A N_A)$ as an error in the background subtraction of each group according to its angular size and redshift (to link M_r and m_r) in the error estimate of the CLF. The test result shows that the errors obtained by including this variance are compa-

rable to the bootstrap errors, indicating that our error estimate is able to deal with effects of galaxy clustering in the background.

3.2. Conditional luminosity functions

We estimate the conditional luminosity functions (CLF) with the method described in subsection 3.1 using the DESI-DR9 imaging data and the SDSS galaxy group catalog described in section 2. In this case, the galaxy property vector \vec{q} is the K -corrected r -band absolute magnitude: $\vec{q} = \{M_r\}$. To minimize observational selection effects, we use a group sample defined as follows. First, any group that has more than 5% of its sky projection outside the DESI-DR9 sky coverage is discarded. This step is achieved by using the random sample provided by the DESI-DR9. Second, we mask out a region around the SDSS Great Wall. The reason for this is that the distribution of galaxy groups in this region is crowded and some of the groups overlap with each other in the sky, making the background subtraction imprecise. Third, we discard any group with $M_h < 10^{13} M_\odot$ that has its center contained in the projection of a more massive group with $M_h \geq 10^{13} M_\odot$. We use 200 bootstrap re-samplings to estimate measurement errors of the conditional luminosity functions. The results of the CLF for galaxies in groups/halos of different masses are shown in Figure 1. Black data points represent results for satellite galaxies while grey data points for central galaxies.

We use analytical models to fit the measured CLF, but for central and satellite galaxies separately. The total CLF at given halo mass can then be given by the sum of the CLF models of centrals and satellites. For central galaxies, we use a Gaussian function,

$$\Phi_c(M) = \frac{1}{\sqrt{2\pi}\sigma} \exp\left[-\frac{(M - \mu)^2}{2\sigma^2}\right], \quad (2)$$

where M is the absolute magnitude, and μ and σ the mean and dispersion of the distribution. We use a Monte Carlo Markov Chain (MCMC) method for the fitting, with each data point weighted by the uncertainty obtained from bootstrap re-sampling. The fitting results are shown as the solid green lines in Figure 1, and the corresponding fitting parameters are listed in Table 1 for reference. The relation between μ and M_h obtained here is in general agreement with that obtained before (e.g. Yang et al. 2009; Lan et al. 2016).

To fit the CLF for satellite galaxies, we use different functional forms for the bright end ($M_r < -18$) and the faint end ($M_r \geq -18$). For the bright end, we use a Schechter function,

$$\Phi_b(M) = N_b \times 10^{-0.4(M - M_b^*)(\alpha_b + 1)} \exp\left[-10^{-0.4(M - M_b^*)}\right], \quad (3)$$

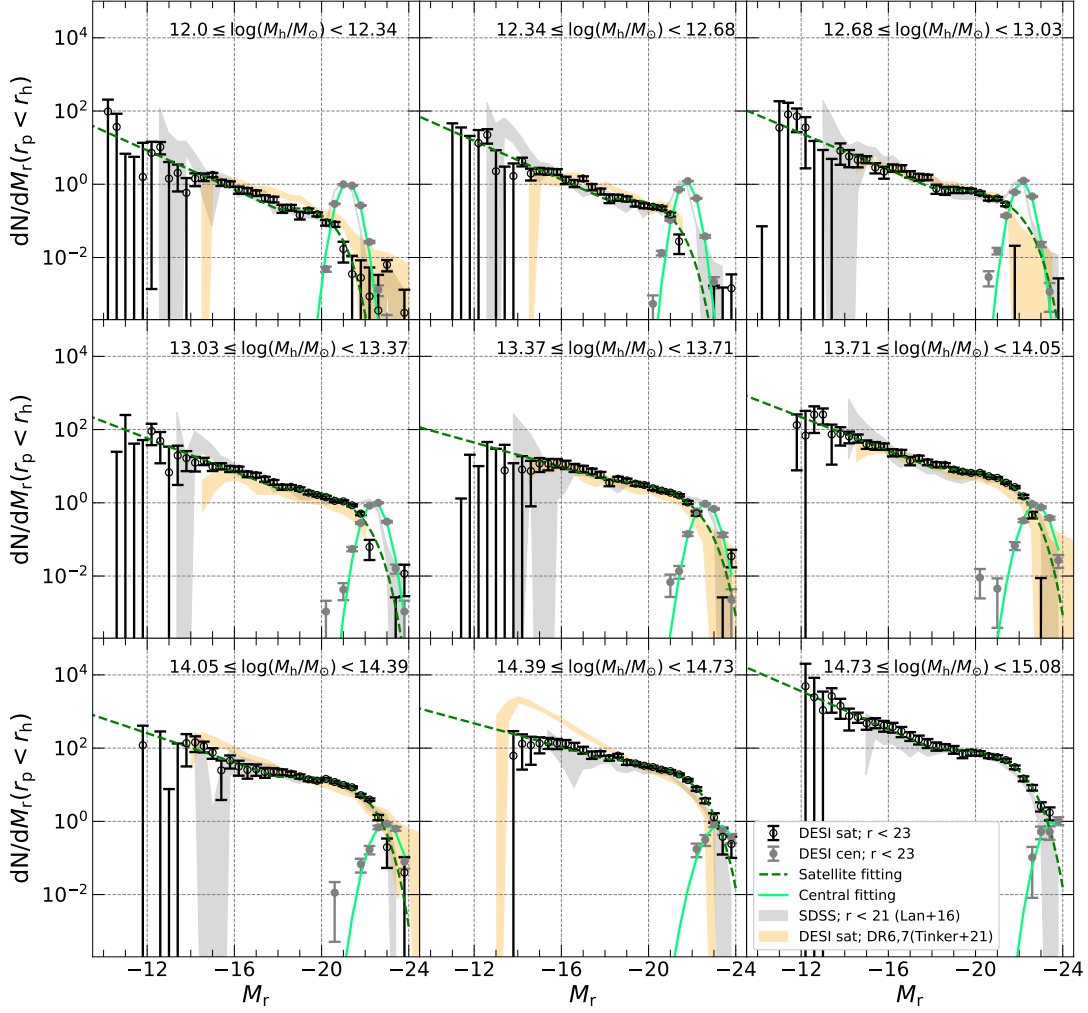


Figure 1. The grey and black dots represent our measurements of the luminosity functions for central galaxies and satellite galaxies in galaxy groups at $0.01 \leq z \leq 0.08$ with the DESI imaging data. The grey shaded regions represent the results of total luminosity functions in galaxy groups in the redshift range $0.01 < z < 0.05$ obtained by Lan et al. (2016) using SDSS imaging data. The orange shaded regions represent the results of the luminosity function of satellite galaxies obtained from Tinker et al. (2021) using the DESI-DR6,7 imaging data. The green solid and dash lines are the fitting results for our central and satellite luminosity functions respectively.

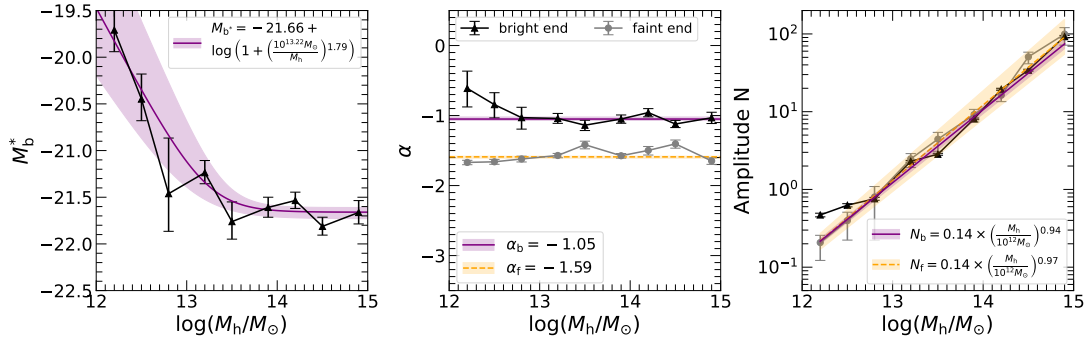


Figure 2. The figures show the model parameters for fitting the conditional luminosity functions of the whole sample as the function of halo mass. The errorbars represent the $1\text{-}\sigma$ scatters of the parameters. The black and grey dots show the results for the bright end and faint end. We choose the proper function forms to describe the dependence of the parameters on the halo mass. The functions are written in the figures shown as the purple and orange lines for the bright and faint end respectively.

where M_b^* is a characteristic magnitude, α_b the faint end slope and N_b an overall amplitude. For the faint end, we use a power law function,

$$\Phi_f(M) = N_f \times 10^{-0.4(M-M_f^*)(\alpha_f+1)}, \quad (4)$$

where M_f^* is a characteristic magnitude, α_f the power index and N_f an overall amplitude. We find the fitting result is insensitive to the chosen value of M_f^* , and so we fix it to be $M_f^* = -18$ to reduce the number of free parameters. We use these functional forms to model the conditional luminosity function of satellite galaxies, instead of the double Schechter function adopted by L16, to reduce the degeneracy between model parameters. We note that we obtained consistent results when using a double Schechter function to fit the data. The functional forms and the separation at $M_r = -18$ are motivated by an inspection of the measured CLF, and the model fits are aimed at providing a compact description of the CLF measurements.

The fitting model adopted here contains five parameters: the bright end amplitude N_b , the characteristic magnitude for the bright end M_b^* , the slope for the bright end α_b , the faint end amplitude N_f and the faint end power index α_f . We require that Φ_b and Φ_f join continuously at $M_r = -18$, so that we have a constraint on the model parameters:

$$\Phi_b(-18) = \Phi_f(-18). \quad (5)$$

Thus, the model is completely specified by four free parameters. Here again, we use the MCMC method to fit the measured CLF of satellite galaxies to the model. The results are shown as green dashed lines in Figure 1 for groups/halos of different mass. As one can see, the functional forms adopted can fit the observational results very well. The best-fit values and the errors of the model parameters are shown in Figure 2 and listed in Table 1. The amplitudes of the CLF, N_f and N_b , increase almost linearly with halo mass, as shown by the fitting results presented in the right panel. The characteristic magnitude, M_b^* , is almost independent of M_h at $M_h > 10^{13}M_\odot$, but becomes significantly fainter at lower M_h . This M_h -dependence of M_b^* is well described by the functional form indicated in the left panel. Both of the slopes, α_b and α_f , are quite independent of halo mass, and α_f is significantly steeper than α_b (see the middle panel). We notice that the faint-end slope, almost constant at $\alpha_f = -1.59$, is very close to the faint-end slope of the luminosity function of the general population of low- z galaxies which is $\alpha \sim -1.6$ after the cosmic variance in the SDSS sample is corrected (Li et al. 2022, see their Figure 8).

3.3. Dependence on galaxy color

In this subsection, we examine the rest-frame color distribution as a function of absolute magnitude for member galaxies of groups/halos. In this case, the galaxy property vector is $\vec{q} = \{M_r, g - z\}$, where the $(g - z)$ color can be obtained from DESI-DR9. Let us first look at all member galaxies in groups with $M_h \geq 10^{12}M_\odot$ at $0.01 \leq z \leq 0.08$. The black data points in Figure 3 show the $(g - z)$ color distributions for group galaxies in different intervals of M_r . As one can see, over a large range of M_r , the color distributions are bimodal. We use a bi-Gaussian function to fit each of the distributions, and the fitting results are shown as colored curves in Figure 3. The red and blue curves are for red and blue modes, respectively, while the green curves are the sum of the two. It is clear that a bi-Gaussian function can fit the observational data very well, and we can use the fitting results to divide galaxies into two populations. For example, one may use the point where the two Gaussian curves intersect to separate galaxies into red and blue populations for each M_r bin. This separation is marked by the vertical dashed line in each panel of Figure 3. Qualitatively, as the luminosity of galaxies decreases, the red fraction first decreases, reaching the lowest value at $M_r \sim -18$, and then increases. In the faint end ($M_r > -15$), almost all galaxies are contained in the red population. We will discuss the results in more detail in section 4.

In Figure 4, we plot the $(g - r)$ color as a function of M_r . The red and blue lines represent the mean values of the Gaussian fitting for the two modes, while the shaded regions represent the corresponding $1-\sigma$ ranges. The green crosses are the separation points shown by the vertical lines in Figure 3. We also obtain a demarcation line following Baldry et al. (2004):

$$T(M_r) = p_0 + q_0 \tanh\left(\frac{M_r - q_1}{q_2}\right). \quad (6)$$

To reduce degeneracy between parameters, we set $q_1 = -15$ and $q_2 = 5$, treating only p_0 and q_0 as free parameters. For a given choice of demarcation (i.e. for given p_0 and q_0), we calculate a ‘completeness’ factor, \mathcal{C}_r or \mathcal{C}_b , which is defined as the fraction of galaxies in the red or blue mode that are selected according to the demarcation line, and a ‘reliability’ factor, \mathcal{R}_r or \mathcal{R}_b , defined as the fraction among all galaxies separated into the red or blue mode by the demarcation line that are truly red or blue mode galaxies. These two factors are estimated for each of the M_r -samples, i , and we compute the value of

$$\mathcal{P} \equiv \prod_i \mathcal{C}_{r,i} \mathcal{R}_{r,i} \mathcal{C}_{b,i} \mathcal{R}_{b,i} \quad (7)$$

Table 1. Model parameters of CLF for the whole sample

$\log(M_h/M_\odot)$	μ	σ	N_b	M_b^*	α_b	N_f	α_f
12.00~ 12.34	$-21.199^{+0.002}_{-0.002}$	$0.339^{+0.001}_{-0.001}$	$0.47^{+0.03}_{-0.03}$	$-19.70^{+0.23}_{-0.25}$	$-0.61^{+0.26}_{-0.25}$	$0.21^{+0.05}_{-0.09}$	$-1.67^{+0.03}_{-0.03}$
12.34~ 12.68	$-21.729^{+0.003}_{-0.003}$	$0.314^{+0.003}_{-0.002}$	$0.62^{+0.03}_{-0.03}$	$-20.45^{+0.23}_{-0.27}$	$-0.84^{+0.19}_{-0.17}$	$0.40^{+0.11}_{-0.17}$	$-1.66^{+0.04}_{-0.03}$
12.68~ 13.03	$-22.150^{+0.005}_{-0.004}$	$0.319^{+0.003}_{-0.003}$	$0.76^{+0.03}_{-0.03}$	$-21.46^{+0.40}_{-0.60}$	$-1.03^{+0.16}_{-0.15}$	$0.80^{+0.29}_{-0.58}$	$-1.62^{+0.04}_{-0.04}$
13.03~ 13.37	$-22.413^{+0.008}_{-0.007}$	$0.368^{+0.005}_{-0.005}$	$2.30^{+0.06}_{-0.06}$	$-21.24^{+0.12}_{-0.13}$	$-1.04^{+0.07}_{-0.07}$	$2.47^{+0.42}_{-0.56}$	$-1.57^{+0.03}_{-0.03}$
13.37~ 13.71	$-22.601^{+0.011}_{-0.011}$	$0.388^{+0.006}_{-0.007}$	$2.84^{+0.08}_{-0.08}$	$-21.76^{+0.19}_{-0.21}$	$-1.14^{+0.08}_{-0.07}$	$4.43^{+0.99}_{-1.33}$	$-1.42^{+0.06}_{-0.05}$
13.71~ 14.05	$-22.777^{+0.016}_{-0.015}$	$0.429^{+0.021}_{-0.018}$	$8.07^{+0.19}_{-0.20}$	$-21.61^{+0.11}_{-0.11}$	$-1.05^{+0.06}_{-0.06}$	$9.18^{+1.52}_{-1.82}$	$-1.57^{+0.03}_{-0.03}$
14.05~ 14.39	$-22.946^{+0.025}_{-0.024}$	$0.422^{+0.021}_{-0.020}$	$19.46^{+0.53}_{-0.54}$	$-21.53^{+0.09}_{-0.09}$	$-0.96^{+0.06}_{-0.06}$	$16.32^{+2.48}_{-2.85}$	$-1.50^{+0.07}_{-0.06}$
14.39~ 14.73	$-23.189^{+0.084}_{-0.115}$	$0.610^{+0.137}_{-0.095}$	$34.21^{+0.93}_{-0.93}$	$-21.81^{+0.09}_{-0.10}$	$-1.12^{+0.05}_{-0.05}$	$50.73^{+7.52}_{-9.44}$	$-1.40^{+0.06}_{-0.06}$
14.73~ 15.08	$-23.710^{+0.152}_{-0.180}$	$0.535^{+0.172}_{-0.106}$	$92.37^{+3.47}_{-3.36}$	$-21.66^{+0.12}_{-0.13}$	$-1.03^{+0.08}_{-0.08}$	$99.37^{+21.10}_{-27.68}$	$-1.65^{+0.05}_{-0.04}$

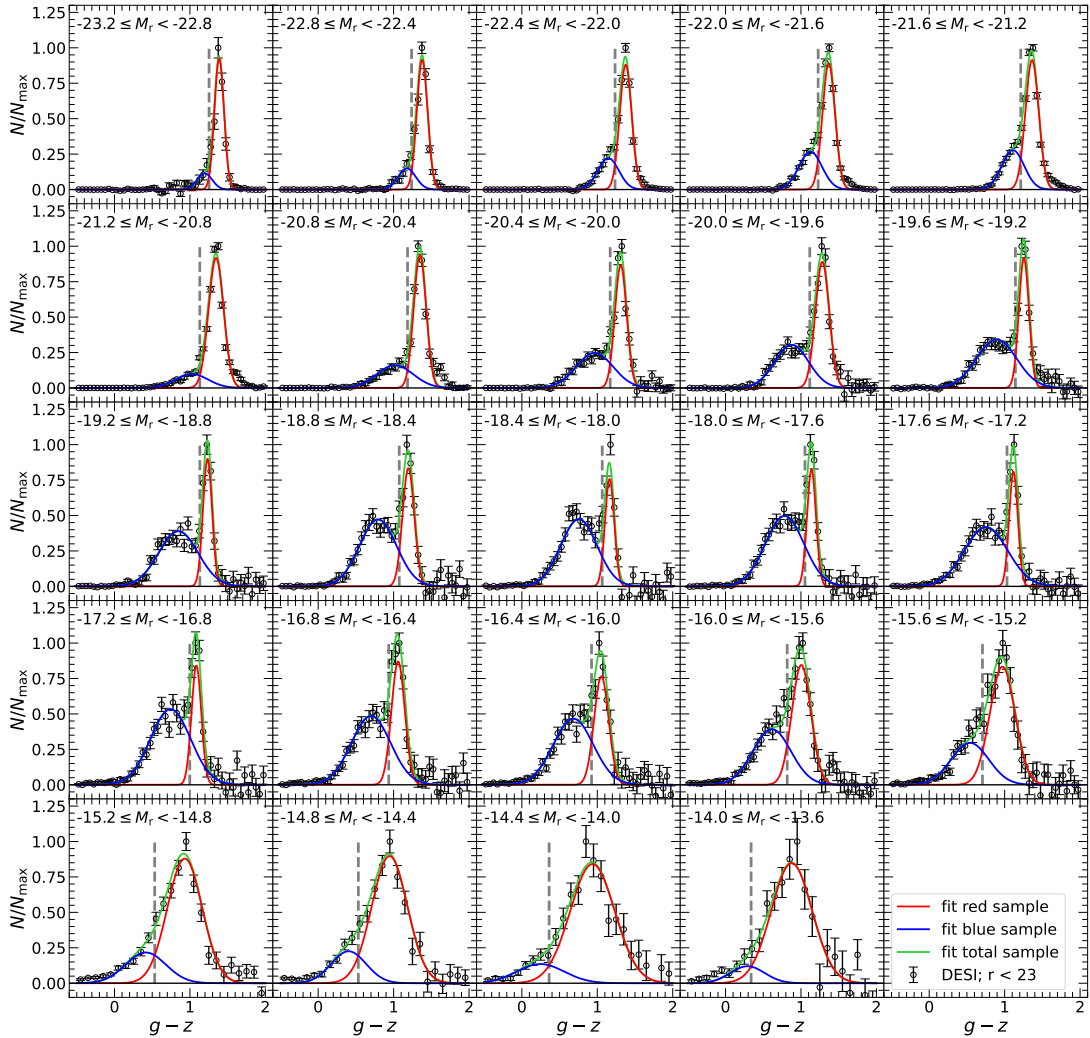


Figure 3. The black dots represent the $(g-z)$ color distributions of all member galaxies in the galaxy groups with $M_h > 10^{12} M_\odot$ at $0.01 < z < 0.08$ using DESI imaging data. The red and blue solid lines are the fitting results with Gaussian function for the red sequence and blue sequence. The green lines are the overall fitting results. The grey vertical dash lines are the dividing lines to separate the red and blue populations.

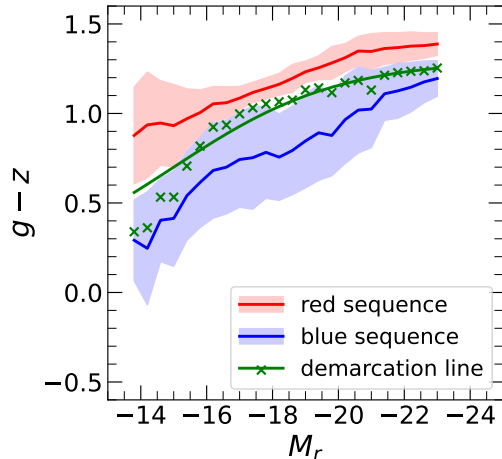


Figure 4. Here we show the fitted red and blue sequence in Fig. 3 for $(g - z)$ color as the function of absolute magnitude. The solid lines represent the mean value and the shade region represent the $1\text{-}\sigma$ scatter of the sequence. The green crosses represent the demarcation points at given absolute magnitude. The green solid line are the fitted demarcation line of Eq. 8.

for the set of parameters in question, and maximize \mathcal{P} by varying the values of p_0 and q_0 . The optimized color demarcation line so obtained is

$$T(M_r) = 0.7 - 0.6 \tanh\left(\frac{M_r + 15}{5}\right), \quad (8)$$

which is shown as the green line in Figure 4. This demarcation line matches that represented by the green crosses well at $M_r < -15$. From Figure 3 we can see that both the red and blue modes become broad and overlap with each other at $M_r > -15$, making it difficult to have a clean separation of the two modes. However, our tests showed that this uncertainty in the color demarcation does not have a significant impact on our results.

We use Equation 8 to divide group galaxies into red and blue populations and compute the CLF separately for them. The results are shown in Figure 5 and Figure 6 for the blue and red populations, respectively. The light blue (red) and dark blue (red) data points represent the results of central and satellite galaxies in the blue (red) population. For blue satellites, the CLF can be well fitted by a single Schechter function. The fitting results are shown as dashed green lines in Figure 5, and the corresponding fitting parameters are shown as functions of halo mass in the upper panels of Figure 7 and are listed in Table 2 for reference. As one can see, the single Schechter model describes the data well.

We use the same power-law plus Schechter model described in subsection 3.2 to fit the CLF for red satellites, and the fitting results are shown as dashed green lines

in Figure 6. The fitting parameters are plotted as functions of halo mass in the lower panels of Figure 7 and are listed in Table 2 for reference. We again see that the fitting model describes well all the observed CLF of the red population. For reference, we use the same functional forms described in subsection 3.2 to fit the dependence of the model parameters on halo mass. The results are shown in Figure 7 and the corresponding fitting functions are provided in each panel.

As one can see from Figure 7, the faint-end slope for the CLF of the blue population, $\alpha \approx -1.25$, is almost completely independent of halo mass. This is also true for the brighter (Schechter) portion of the CLF of the red population, although the slope, $\alpha_b \approx 0.8$ is much shallower. The faint, power-law portion of the CLF for the red population has a slope, $\alpha_f \sim -1.8$, although there are some fluctuations from sample to sample. For the blue population, the characteristic absolute magnitude is roughly a constant, $M_b^* \sim -21.1$, for halos with $M_h > 10^{13} M_\odot$, and increases (becomes fainter) with decreasing M_h at $M_h < 10^{13} M_\odot$. The dependence of M_b^* on halo mass for the Schechter portion of the red population is roughly the same as the blue population, although the errors in the measurements are much larger at the low- M_h end. At a given M_h , the characteristic absolute magnitude for the red population is in general brighter than that for the blue population. Finally, the overall amplitude of the CLF is roughly a power-law for both populations, but it is sub-linear, with a power index of ~ 0.7 , for blue galaxies, and slightly super-linear, with a power index of ~ 1.1 , for the red population. These results are consistent with those obtained previously, as we will discuss in the following subsection.

3.4. Comparison with previous results

For comparison, the shaded grey regions in Figure 1, Figure 5 and Figure 6 show the CLF measurements obtained by L16 from the SDSS imaging data, and the shaded orange regions in Figure 1 show the measurements by Tinker et al. (2021) from the DESI DR6 and DR7 imaging data. As one can see, our measurements match both of the previous results. For the total CLFs, the only exception is seen at $14.39 \leq \log(M_h/M_\odot) < 14.73$, where the CLF obtained by Tinker et al. (2021) is higher at $M_r > -19$. The reason is that Tinker et al. (2021) included all massive groups in this mass bin, but L16 and our work have one more mass bin for the most massive groups as shown in the bottom-right panel. Since DESI-DR9 is about 2 magnitudes deeper than the SDSS data and DESI-DR9 has more pass times

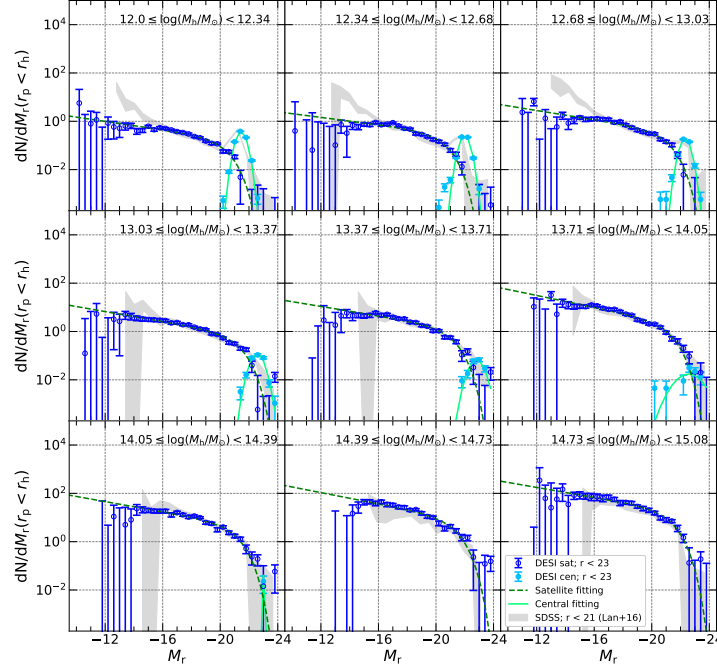


Figure 5. The dark blue hollow dots and light blue solid dots represent our measurements of the luminosity functions for central galaxies and satellite galaxies of blue sample in galaxy groups at $0.01 \leq z \leq 0.08$ with the DESI imaging data. The grey shaded regions represent the results of total luminosity functions in galaxy groups for the blue sample in the redshift range $0.01 < z < 0.05$ obtained by L16 using SDSS imaging data. The green solid and dash lines are the fitting results for our central and satellite luminosity functions respectively.

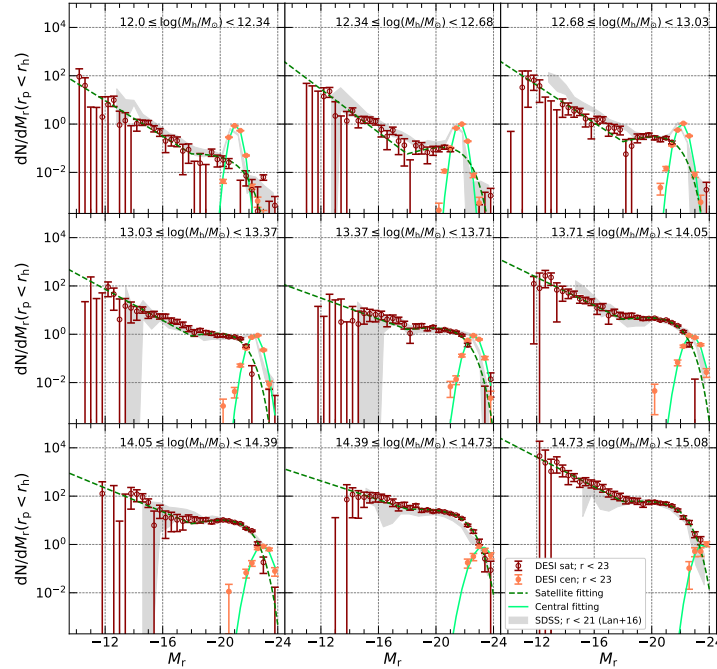


Figure 6. The dark red hollow dots and light red solid dots represent our measurements of the luminosity functions for central galaxies and satellite galaxies of red sample in galaxy groups at $0.01 \leq z \leq 0.08$ with the DESI imaging data. The grey shaded regions represent the results of total luminosity functions in galaxy groups for the red sample in the redshift range $0.01 < z < 0.05$ obtained by L16 using SDSS imaging data. The green solid and dash lines are the fitting results for our central and satellite luminosity functions respectively.

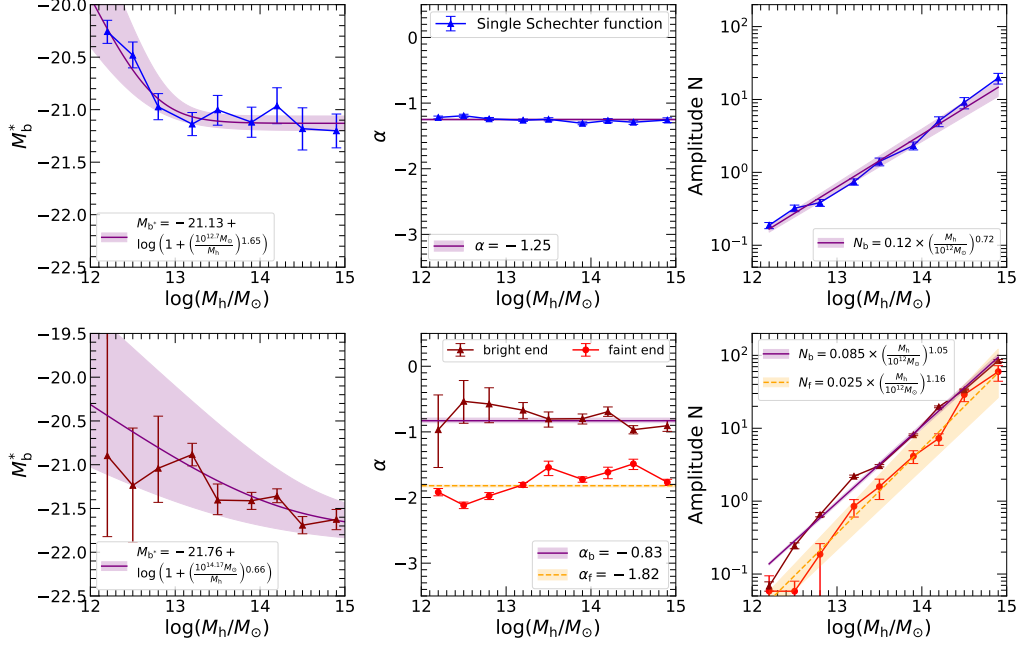


Figure 7. The figures show the model parameters for fitting the conditional luminosity functions of the red sample and blue sample as the function of halo mass. The errorbars represent the $1\text{-}\sigma$ scatters of the parameters. We choose the same function forms as in Fig. 2 to describe the dependence of the parameters on the halo mass. The functions are written in the figures, shown as the purple and orange lines for the bright and faint end respectively.

Table 2. Model parameters of CLF for red and blue sample

$\log(M_h/M_\odot)$	μ	σ	N_b	M_b^*	α_b	N_f	α_f
red							
12.00~ 12.34	$-21.085^{+0.002}_{-0.002}$	$0.296^{+0.001}_{-0.001}$	$0.06^{+0.01}_{-0.01}$	$-20.90^{+0.92}_{-1.60}$	$-0.97^{+0.58}_{-0.53}$	$0.06^{+0.04}_{-0.39}$	$-1.92^{+0.06}_{-0.06}$
12.34~ 12.68	$-21.666^{+0.003}_{-0.003}$	$0.298^{+0.003}_{-0.003}$	$0.25^{+0.02}_{-0.02}$	$-21.24^{+0.65}_{-0.66}$	$-0.53^{+0.33}_{-0.32}$	$0.06^{+0.02}_{-0.07}$	$-2.12^{+0.05}_{-0.05}$
12.68~ 13.03	$-22.113^{+0.005}_{-0.005}$	$0.309^{+0.003}_{-0.003}$	$0.65^{+0.04}_{-0.04}$	$-21.04^{+0.39}_{-0.60}$	$-0.58^{+0.29}_{-0.25}$	$0.19^{+0.07}_{-0.14}$	$-1.97^{+0.06}_{-0.06}$
13.03~ 13.37	$-22.392^{+0.007}_{-0.008}$	$0.356^{+0.005}_{-0.005}$	$2.20^{+0.08}_{-0.08}$	$-20.88^{+0.13}_{-0.13}$	$-0.67^{+0.13}_{-0.12}$	$0.85^{+0.20}_{-0.25}$	$-1.81^{+0.04}_{-0.04}$
13.37~ 13.71	$-22.592^{+0.011}_{-0.011}$	$0.391^{+0.007}_{-0.007}$	$3.06^{+0.11}_{-0.11}$	$-21.40^{+0.17}_{-0.18}$	$-0.80^{+0.12}_{-0.11}$	$1.58^{+0.42}_{-0.53}$	$-1.54^{+0.12}_{-0.10}$
13.71~ 14.05	$-22.778^{+0.017}_{-0.016}$	$0.413^{+0.012}_{-0.012}$	$8.13^{+0.21}_{-0.23}$	$-21.41^{+0.10}_{-0.10}$	$-0.80^{+0.08}_{-0.07}$	$4.14^{+0.78}_{-0.86}$	$-1.72^{+0.04}_{-0.04}$
14.05~ 14.39	$-22.943^{+0.028}_{-0.026}$	$0.429^{+0.022}_{-0.021}$	$19.68^{+0.57}_{-0.57}$	$-21.36^{+0.08}_{-0.08}$	$-0.69^{+0.07}_{-0.07}$	$7.26^{+1.12}_{-1.43}$	$-1.61^{+0.10}_{-0.08}$
14.39~ 14.73	$-23.182^{+0.079}_{-0.095}$	$0.594^{+0.140}_{-0.093}$	$33.64^{+0.99}_{-1.00}$	$-21.69^{+0.10}_{-0.10}$	$-0.97^{+0.06}_{-0.06}$	$29.01^{+4.84}_{-5.84}$	$-1.49^{+0.09}_{-0.07}$
14.73~ 15.08	$-23.720^{+0.170}_{-0.201}$	$0.553^{+0.202}_{-0.117}$	$84.59^{+3.24}_{-3.20}$	$-21.62^{+0.12}_{-0.11}$	$-0.91^{+0.09}_{-0.08}$	$59.75^{+12.42}_{-15.58}$	$-1.77^{+0.05}_{-0.05}$
blue							
12.00~ 12.34	$-21.455^{+0.004}_{-0.004}$	$0.314^{+0.003}_{-0.003}$	$0.19^{+0.02}_{-0.02}$	$-20.26^{+0.11}_{-0.11}$	$-1.22^{+0.02}_{-0.02}$		
12.34~ 12.68	$-21.995^{+0.006}_{-0.006}$	$0.289^{+0.005}_{-0.005}$	$0.32^{+0.03}_{-0.03}$	$-20.48^{+0.12}_{-0.13}$	$-1.19^{+0.02}_{-0.02}$		
12.68~ 13.03	$-22.330^{+0.012}_{-0.012}$	$0.300^{+0.009}_{-0.009}$	$0.38^{+0.04}_{-0.04}$	$-20.97^{+0.12}_{-0.13}$	$-1.24^{+0.02}_{-0.02}$		
13.03~ 13.37	$-22.566^{+0.022}_{-0.023}$	$0.388^{+0.015}_{-0.016}$	$0.74^{+0.08}_{-0.07}$	$-21.14^{+0.11}_{-0.11}$	$-1.26^{+0.02}_{-0.02}$		
13.37~ 13.71	$-22.865^{+0.057}_{-0.063}$	$0.453^{+0.081}_{-0.058}$	$1.41^{+0.18}_{-0.16}$	$-21.00^{+0.15}_{-0.14}$	$-1.25^{+0.02}_{-0.02}$		
13.71~ 14.05	$-22.561^{+0.184}_{-0.187}$	$0.783^{+0.182}_{-0.377}$	$2.33^{+0.30}_{-0.28}$	$-21.13^{+0.14}_{-0.14}$	$-1.31^{+0.02}_{-0.02}$		
14.05~ 14.39	$-23.039^{+0.077}_{-0.077}$	$0.077^{+0.039}_{-0.038}$	$5.08^{+0.85}_{-0.70}$	$-20.96^{+0.17}_{-0.17}$	$-1.27^{+0.03}_{-0.03}$		
14.39~ 14.73			$9.14^{+1.70}_{-1.46}$	$-21.18^{+0.21}_{-0.20}$	$-1.29^{+0.03}_{-0.03}$		
14.73~ 15.08			$19.74^{+3.47}_{-3.08}$	$-21.20^{+0.16}_{-0.16}$	$-1.26^{+0.04}_{-0.03}$		

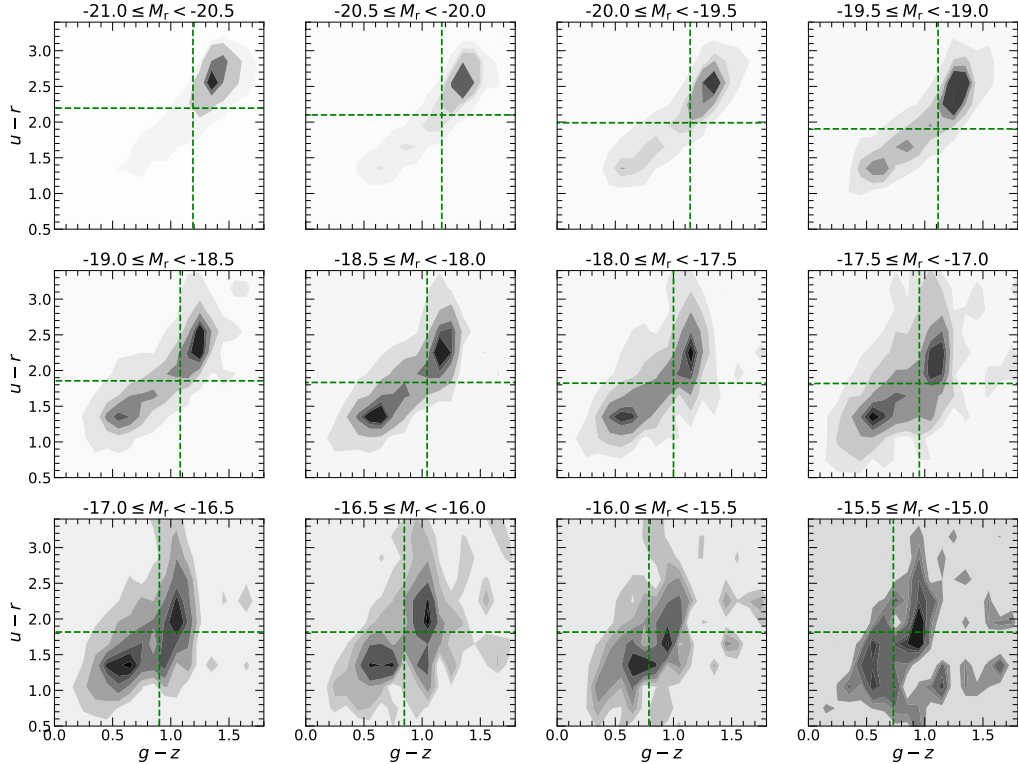


Figure 8. The color-color diagram in $(g-z)$ - $(u-r)$ space for all member galaxies in the groups with DESI imaging data at different absolute magnitude. The green dash lines are the demarcation lines to separate the red and blue mode. The demarcation lines for $(g-z)$ color are from Equation 8. The demarcation lines for $(u-r)$ color are from Baldry et al. (2004).

than the DESI-DR6/7, our measurements have smaller uncertainties than those obtained by L16 and Tinker et al. (2021).

Another discrepancy can be seen in the low-luminosity ends ($M_r > -16$) of the CLF in low-mass halos ($M_h < 10^{13} M_\odot$), particularly for the blue population, where a significant upturn is seen in L16 but absent in ours. This might be attributed to the fact that L16 used the SDSS $(u-r)$ color, instead of the $(g-z)$ color used here, to separate galaxies into blue and red populations. In Figure 8, we show the distribution of group galaxies in the $(u-r)$ versus $(g-z)$ diagram, where the $(u-r)$ color is from the SDSS photometry used in L16 while the $(g-z)$ color is from the DESI-DR9 photometry used in our analyses. Group members are identified from the DESI-DR9 using the method described in subsection 3.1 and are matched to SDSS galaxies using their centroid positions (RA, Dec). Only galaxies brighter than the SDSS magnitude limit of $r < 21$ are used. For comparison, the horizontal lines show the demarcations of red and blue populations adopted by L16, while the vertical lines are those adopted in the present paper. For $M_r < -17$, the distribution is bimodal in both $(u-r)$ and $(g-z)$, and the demarcations adopted by L16 and us give similar separations of the two populations. For

fainter galaxies with $M_r > -17$, a bimodal distribution can still be seen in the $(g-z)$ color and is delineated by our demarcation lines, but it is much less clear in the $(u-r)$ distribution. The demarcations adopted by L16 cut across the red modes, which might explain the strong upturn in the faint end of the CLF obtained by L16 for blue galaxies in low-mass groups. There are also some differences in the fitting parameters between our results and those of L16. For low-mass halos, the characteristic magnitudes of the CLF from our fitting are slightly fainter. The bright ends of the CLF for satellite galaxies in these low-mass halos are quite noisy. The fitting results of L16 sometimes extend to the range of M_r where the measurements of the CLF for satellite galaxies drop rapidly to zero, while our fitting results follow this rapid drop more closely. We note that there is degeneracy among model parameters, and that our fitting functions can match the measurements from the SDSS imaging data, as one can see in Figure 1, Figure 5 and Figure 6.

4. THE OLD AND YOUNG POPULATIONS OF SATELLITE GALAXIES

4.1. The presence of an old sequence

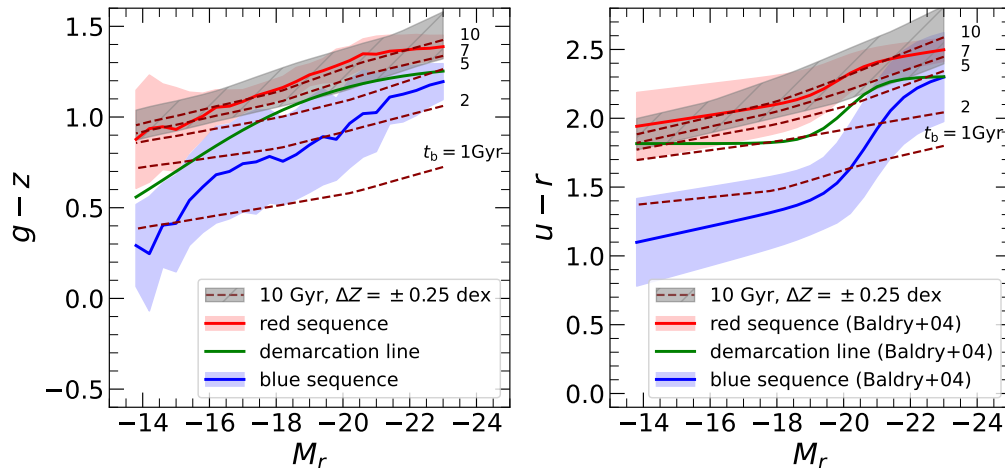


Figure 9. The figures show the red and blue sequence as the function of absolute magnitude for $(g - z)$ and $(u - r)$ color. The sequences for $(g - z)$ are same as Figure 4 and the sequences for $(u - r)$ are from Baldry et al. (2004). The dark red lines represent the results of the single burst model. The look-back time of the star burst are labelled on the figure.

As shown in Figure 3, group galaxies have bimodal distributions in their $(g - z)$ colors. At the very bright end, the population is dominated by galaxies in a narrow $(g - z)$ color distribution in the red component. As galaxy luminosity decreases, the peak position of the red component of the distribution shifts gradually towards the blue end, with the width remaining roughly constant for $M_r < -16$ and becoming broader for fainter galaxies. Starting from the brightest end, the blue component becomes more important for fainter galaxies. The importance of the blue component reaches its maximum at $M_r \sim -18$ and decreases gradually towards the fainter end. We note that the red and blue modes start to merge at $M_r > -16$, and the blue modes are observed only as an extended tail at the blue side of the $(g - z)$ distribution. We also note that the red modes for faint galaxies are actually bluer than the blue modes for galaxies at the brightest end. Thus, our separation of red and blue populations is not in terms of absolute color, but based on the bimodal distribution of galaxies of similar luminosity.

To gain insights into potential causes of the color bimodality of group galaxies, we use the BC03 spectral synthesis model (Bruzual & Charlot 2003) assuming the Chabrier initial mass function (Chabrier 2003) to provide some guidance. We first consider a simple case where the star formation history is a single burst at some look-back time t_b :

$$\Psi(t) \propto \delta(t - t_b), \quad (9)$$

where t is the cosmic look-back time. The spectrum of a stellar population depends not only on the stellar age, but also on the stellar metallicity. We use the observed mass-metallicity relation (MZR) given in Kirby et al.

(2013) to model the metallicity:

$$\log\left(\frac{Z}{Z_\odot}\right) = (-1.69 \pm 0.04) + (0.30 \pm 0.02) \log\left(\frac{M_*}{10^6 M_\odot}\right), \quad (10)$$

where $Z_\odot = 0.02$ and M_\odot are the solar metallicity and mass, respectively. Note that the errors quoted here are uncertainties in the mean relation. The scatter in $\log(Z)$ at given M_* is about 0.25 dex. To obtain the stellar mass of a galaxy from its luminosity, we use the relation between the mass-to-light ratio and color given in Bell et al. (2003):

$$\log\left(\frac{M_*}{M_\odot}\right) = -0.22 + 0.51 \times (g - z) - 0.40 \times (M_r - 4.64) - 0.15, \quad (11)$$

and

$$\log\left(\frac{M_*}{M_\odot}\right) = -0.22 + 0.30 \times (u - r) - 0.40 \times (M_r - 4.64) - 0.15. \quad (12)$$

The single burst model is expected to be valid only for galaxies dominated by old stellar populations. We thus use the $(g - z)$ and $(u - r)$ colors of the red sequence shown in Figure 9 to convert luminosity to stellar mass. We then use Equation 10 to obtain the stellar metallicity. The BC03 model only provides spectra for stellar populations with metallicity $Z = 0.0001, 0.0004, 0.004, 0.008, 0.02$ and 0.05 . To predict the color of the stellar population at the metallicity obtained from the mass-metallicity relation, we first obtain the $(g - z)$ and $(u - r)$ colors of the stellar populations of different ages for each of the 6 metallicities, we then use a linear interpolation to obtain the two colors corresponding to the metallicity in question.

The color-magnitude relations predicted by the single burst model with different ages are presented in Figure 9 as the dashed lines, with the left and right panels

showing results for the $(g - z)$ and $(u - r)$ colors, respectively. The dark shade around the 10 Gyr line in each panel indicates the range covered by the variance of ± 0.25 dex in the metallicity. Also included in the figure are observed color-magnitude relations for both the red and blue sequences obtained in subsection 3.3 for the $(g - z)$ versus M_r relation, and by Baldry et al. (2004) for the $(u - r)$ versus M_r relation. The green lines are the demarcation lines between the red and blue modes. As one can see, the red sequences in both $(g - z)$ and $(u - r)$ are consistent with the prediction of a single burst with an old age ~ 10 Gyr. Both the slope and width of the red sequence follow the prediction of the observed mass-metallicity relation, indicating that the red sequence is dominated by galaxies with an old stellar population, quite independent of the stellar mass of galaxies. The demarcation lines divide the galaxy population roughly at an age around 5 Gyr. However, the shapes of the demarcation lines are quite different from those of the color-magnitude relations predicted by the single burst model, indicating that the star formation history of galaxies becomes more complicated and likely mass-dependent as one moves to the blue sequence.

Next, we consider a more complex model in which the star formation history of a galaxy consists of two components, one starburst in early times, and a constant star formation rate from some earlier time to the present day. Mathematically, the history can be written as follows:

$$\Psi(t) \propto (1 - f_y) \delta(t - t_b) + \left(\frac{f_y}{t_{y,o} - t_{y,e}} \right) \mathcal{H}(t_{y,o} - t) \mathcal{H}(t - t_{y,e}), \quad (13)$$

where $\mathcal{H}(t)$ is the step function: $\mathcal{H}(x) = 1$ for $x > 0$ and $= 0$ otherwise; f_y is the fraction of the young population; t_b is the age of the old population; $t_{y,o}$ and $t_{y,e}$ are the look-back times of the onset and ending of the constant star formation period, respectively. For simplicity, we fix the age of the old population at $t_b = 10$ Gyr, and the onset of the young population at $t_{y,o} = 5$ Gyr. We test three cases where $t_{y,e} = 0, 0.1$ and 1.0 Gyr, respectively. We note that our results are not sensitive to the exact values chosen for t_b and $t_{y,o}$. We use the same method as described above for the single burst model to estimate the color-magnitude relations for different values of the young fraction, f_y .

In Figure 10 the triangles show the predicted $(g - z)$ versus $(u - r)$ relation on top of contours showing the observed color-color relation for group galaxies. The three tracks in each panel represent the three different assumptions for the value of $t_{y,e}$, while the color scale along each track represents the value of the young fraction, f_y . In each panel, the open square shows the result of a burst at $t_b = 10$ Gyr, with a metallicity of 0.25 dex above that assumed for the $t_{y,e}$ sequences plot-

ted in the panel. As one can see, the model predictions can roughly cover the color-color sequence for galaxies of different luminosity in the observational data. In particular, the f_y -sequence assuming $t_{y,e} = 0.1$ Gyr follows well the trend from the red to blue modes. Galaxies in the red mode are old in their stellar population, and there is little room for them to contain a significant amount of recent star formation. The blue mode is consistent with having a constant star formation rate continuing to the present day, but more than half of the stellar mass is still contained in the old population, even for low-luminosity galaxies. This is consistent with results obtained by Weisz et al. (2011) from modeling the color-magnitude relation of individual stars in nearby low-mass galaxies, by Lu et al. (2014, 2015) from empirical models of galaxy formation in dark matter halos, and by Zhou et al. (2020) from stellar population synthesis modeling of the star formation history of low-mass galaxies in the SDSS-IV/MaNGA survey. As expected, the allowed young fraction depends on the value of $t_{y,e}$. For $t_{y,e} = 1$ Gyr, the young fraction f_y near the demarcation line is about 30% at $M_r < -17$. In contrast, if $t_{y,e} = 0$, the value of f_y near both demarcation lines are less than 5%. For $M_r > -17$, the value of f_y at the demarcation lines can be a factor of two higher. Overall, a large fraction of stars are still in the old population, independent of galaxy luminosity.

For low-luminosity galaxies, the observed $(u - r)$ color distribution at given $(g - z)$ has large scatter, which is not well reproduced by varying the age and metallicity of the stellar population. We note, however, that the u -band data from the SDSS imaging survey are relatively shallow, with the 95% completeness limit at $u \approx 22.0$ (Abazajian et al. 2009). Thus the results shown in Figure 8, obtained from data at $r < 21$, may be affected significantly by the detection limit of the u -band, particularly for faint red galaxies that are intrinsically faint in ultraviolet. The model presented here is also very simple, and ignores any dust attenuation that may have a significant impact on the $(u - r)$ color. Furthermore, there is also degeneracy between age and metallicity in the spectral synthesis model used here. In our model, we only use the mean metallicity-mass relation to make model predictions. We find that including the scatter in the metallicity-mass relation has the effect of stretching the color-color relation along individual $t_{y,e}$ sequence, without broadening it significantly. However, there might be correlations between metallicity and other galaxy properties, which may change the color-color relation and is not included in our model.

In conclusion, our results indicate that (i) member galaxies of clusters/groups in the red mode are

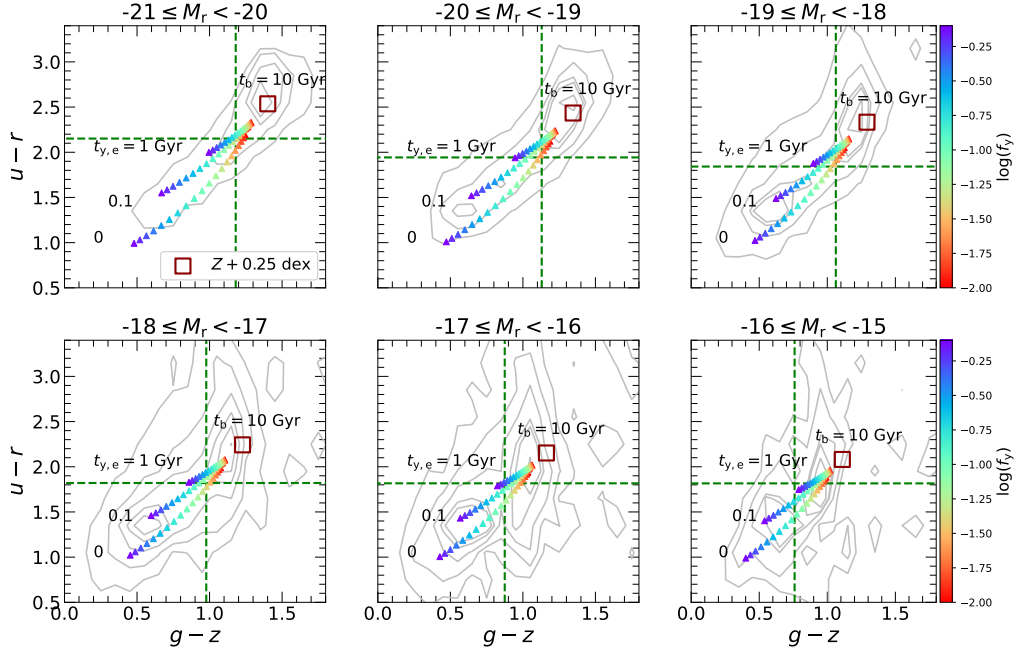


Figure 10. The figures show the results of the two components model, one starburst in early time and a constant star formation rate from some early time to the present day at different absolute magnitude. The age of starburst is $t_b = 10$ Gyr. The constant star formation starts from $t_{y,o} = 5$ Gyr. We plot three cases where $t_{y,e} = 0, 0.1, 1.0$ Gyr. The colors represent the fraction of the young population. The hollow squares represent the results of the starburst model with the metallicity higher than the mean relation of Equation 10 0.25 dex. The background grey contours represent the distribution in the groups we measure.

dominated by old stellar populations, independent of galaxy luminosity (mass); (ii) member galaxies of clusters/groups in the blue mode also contain a large fraction (more than a half) of old stars in their stellar population; (iii) a more-or-less constant star formation extending to the recent past is needed for galaxies, particularly low-luminosity ones, in the blue mode; (iv) for galaxies in the green valley [near demarcation lines in the $(u-r)$ - $(g-z)$ plane], only a small fraction of their stars can have ages lower than 1 Gyr, indicating that their star formation was quenched more than 1 Gyr ago.

4.2. The old fraction and evidence for a characteristic stellar mass scale

In last subsection, we have seen that there is a well-defined population of red galaxies that are old. Here we examine the fraction of the old population as a function of galaxy luminosity (mass) in halos of different mass. The old fraction is calculated from the conditional luminosity function of red galaxies divided by that of the total population, and the results are shown in Figure 11. The red lines are the results obtained from the DESI-DR9, and the shaded regions represent the standard deviation estimated from 200 bootstrap re-samplings. The average old fraction increases with halo mass, particularly in the intermediate luminosity range. There is a valley-like structure of the old fraction as a function of

galaxy luminosity for all halo mass bins. The minimum of the old fraction occurs at $M_r \sim -18$, pretty much independent of halo mass. This result indicates the existence of a characteristic luminosity, $M_r \sim -18$ (corresponding roughly to a stellar mass of $10^{9.5} M_\odot$), at which the old fraction of galaxies is the lowest.

As a check of our results, we also estimate the old fraction using the spectroscopic sample from SDSS, which is much shallower than the DESI-DR9. The memberships of individual galaxy groups used here are adopted directly from Yang et al. (2007). Each galaxy is weighted by $1/(V_{\max}C)$ to compensate the apparent magnitude limit and redshift incompleteness, where V_{\max} and C are both from the NYU-VAGC. The results obtained this way are shown as blue solid points in Figure 11, with error bars again obtained from 200 bootstrap samples. These results are consistent with those obtained from DESI-DR9 over the luminosity range where the old fraction can be measured reliably from the spectroscopic sample. For the lowest three halo mass bins where the measurements from the spectroscopic sample can go below $M_r = -18$, an upturn towards the fainter end can also be seen. All these indicate that the use of the photometric data does not introduce any significant systematic error in our results.

4.3. Comparisons with previous observations

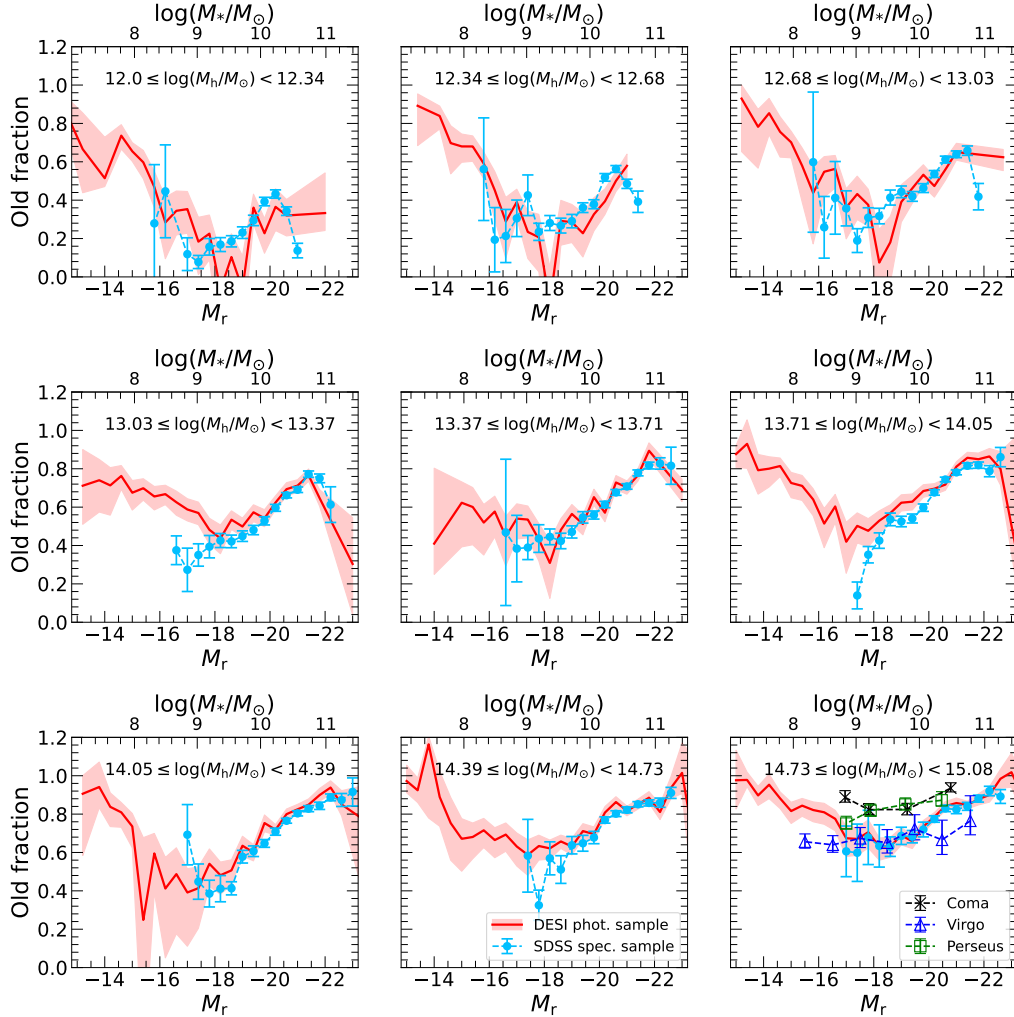


Figure 11. The old fraction defined as the fraction of the satellites in red mode by the $(g - z)$ color as a function of r -band absolute magnitude and stellar mass, measured for different intervals of halo mass as indicated. In each panel the red line shows the measurements from the DESI photometric sample, and the shaded region shows the standard deviation estimated from 200 bootstrap re-samplings. The light blue dots connected by dashed lines represent the result from the SDSS spectroscopic sample. The three additional symbols/lines in the last panel show the red fractions measured by Weinmann et al. (2011) for the Coma, Virgo and Perseus clusters.

There have been many studies to measure the fraction of quenched/red galaxies as functions of galaxy properties and/or dark matter halo mass. In most cases these studies are based on spectroscopic samples limited to relatively bright galaxies, while other studies are focused on individual systems in the nearby Universe. In the bottom-right panel of Figure 11 we show the red fractions measured by Weinmann et al. (2011) for the Coma, Virgo, and Perseus clusters. Similar to our result, the red fraction in Coma cluster shows a dip at around $M_r \sim -18.5$, although the overall amplitude is higher. The red fractions in the Virgo cluster are comparable to our result, but with a weaker dependence on luminosity and no obvious dip at any luminosity. The Perseus cluster also shows no significant dip at the in-

termediate luminosity, and red fractions are comparable to those of the Coma cluster and higher than our result. We note that the red/blue galaxy populations in Weinmann et al. (2011) were identified using the $(g - r)$ color, which might mis-classify some of the faint galaxies that are red in $(g - z)$ but blue in $(g - r)$. The higher red fractions in Coma and Perseus may be reflecting the overall increase of the red fraction with increasing halo mass, given that the halo masses of the two clusters, $M_h = 2.7 \times 10^{15} M_\odot$ for Coma (Kubo et al. 2007) and $M_h = 2.2 \times 10^{15} M_\odot$ for Perseus (Meusinger et al. 2020), are higher than both the average mass of groups in that panel, $M_h = 7 \times 10^{14} M_\odot$, and the mass of the Virgo cluster, $M_h = 6.3 \times 10^{14} M_\odot$ (Kashibadze et al. 2020). Given

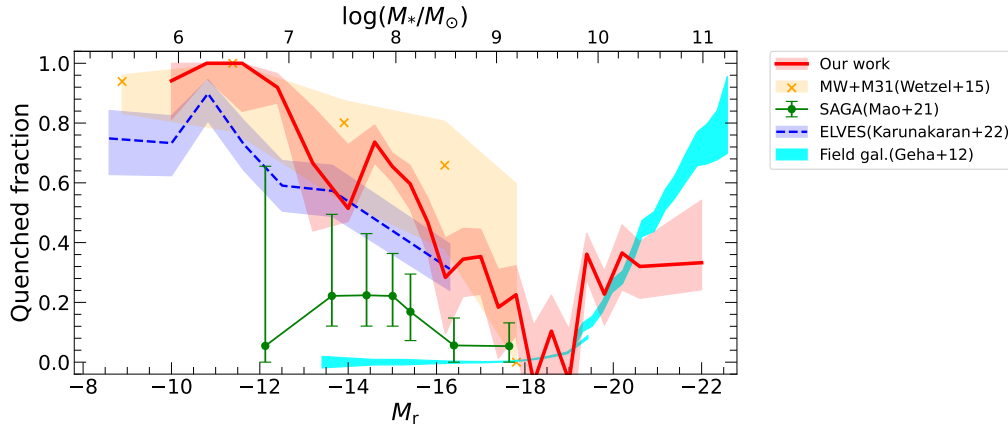


Figure 12. Our measurements of old fraction of satellite galaxies in Milky Way mass halos with $12 \leq \log(M_h/M_\odot) < 12.34$ (red line) is compared with the quenched fraction of the satellites in the Milky Way and M31 system (yellow crosses; Wetzel et al. 2015), as well as measurements from the ELVES (blue dashed line; Karunakaran et al. 2022) and SAGA (green symbols/line; Mao et al. 2021) surveys. The result for field galaxies in SDSS from Geha et al. (2012) is plotted as the cyan shaded region for comparison.

these differences, the comparison with our results is not straightforward.

Measurements of quenched fractions for faint satellite galaxies have also been obtained recently for nearby systems similar to the Local Group. In Figure 12 we show the old fraction of galaxies as a function of M_r obtained by us for Milky Way-like halos with $12.0 \leq (\log(M_h/M_\odot)) < 12.34$, in comparison with the quenched fractions obtained by Wetzel et al. (2015) for the MW+M31 system, by Geha et al. (2017) and Mao et al. (2021) using the SAGA survey of 127 satellite galaxies around 36 Milky Way (MW) analogs at $z \sim 0.01$, and by Carlsten et al. (2022) and Karunakaran et al. (2022) using the ELVES survey of a nearly volume-limited sample of dwarf satellites down to $M_V \sim -9$. Our result is in good agreement with the result of both the MW+M31 halo and the ELVES survey. The quenched fractions from the SAGA survey also show an upturn as the luminosity decreases, but overall they are significantly lower than both the MW+M31 result and our measurement. Karunakaran et al. (2022) made careful comparisons between the SAGA and ELVES results, and attributed the lower quenched fractions from SAGA to sample incompleteness at the low-mass end caused by the adopted absolute magnitude cut for satellites ($M_r < -12.3$). Note, however, the old fraction in the present paper is defined by the $(g-z)$ color, which could be different from the quenched fraction defined in other studies using star formation rates. As mentioned in subsection 4.1, the old sequence based on the $(g-z)$ color may contain some recent star formation, and the true quenched fraction might be lower than the old fraction defined in our paper. For comparison, the quenched fraction of *field* galaxies estimated by Geha et al. (2012) based on the

NASA-Sloan Atlas catalog (Blanton et al. 2011) is plotted as the cyan shaded region. Different from the member galaxies of groups/clusters, galaxies with $M_r > -18$ in the field are barely quenched. This again indicates that the upturn of the old (quenched) fractions at the faint end is a unique behavior of group/cluster galaxies.

4.4. Comparisons with theoretical predictions

It is also interesting to compare our measurements of the old fraction with theoretical models which predict the fraction of quenched or quiescent satellites for halos of different mass. In Figure 13, we compare our measurements with the predictions by two “state-of-the-art” hydro-dynamic simulations: Illustris-TNG100 (Nelson et al. 2019; Pillepich et al. 2018) and EAGLE (Schaye et al. 2015; Crain et al. 2015; McAlpine et al. 2016). For massive galaxies with $M_* \gtrsim 10^{10} M_\odot$, both simulations can roughly match the observational results, consistent with what was found in Xie et al. (2020). Both simulations can also roughly reproduce the Valley-like shape of the quenched fraction, although the minimum of the quenched fraction in the simulations occurs at a slightly higher luminosity ($M_r = -19 \sim -20$) than in the observation ($M_r \sim -18$). Quantitatively, Illustris-TNG100 can match the observation down to $M_* \sim 10^8 M_\odot$ for halos with mass $M_h \lesssim 5 \times 10^{13} M_\odot$, while EAGLE overpredicts the quenched fractions for galaxies below the characteristic mass for halos of all masses except for Milky-Way mass halos. For massive halos above $M_h \sim 5 \times 10^{13} M_\odot$, both simulations significantly over-predict the quenched fraction for satellites with $M_* < 10^{10-10.5} M_\odot$. Our result indicates that quenching mechanisms implemented in current hydro-dynamic simulations are able to capture the evolutionary

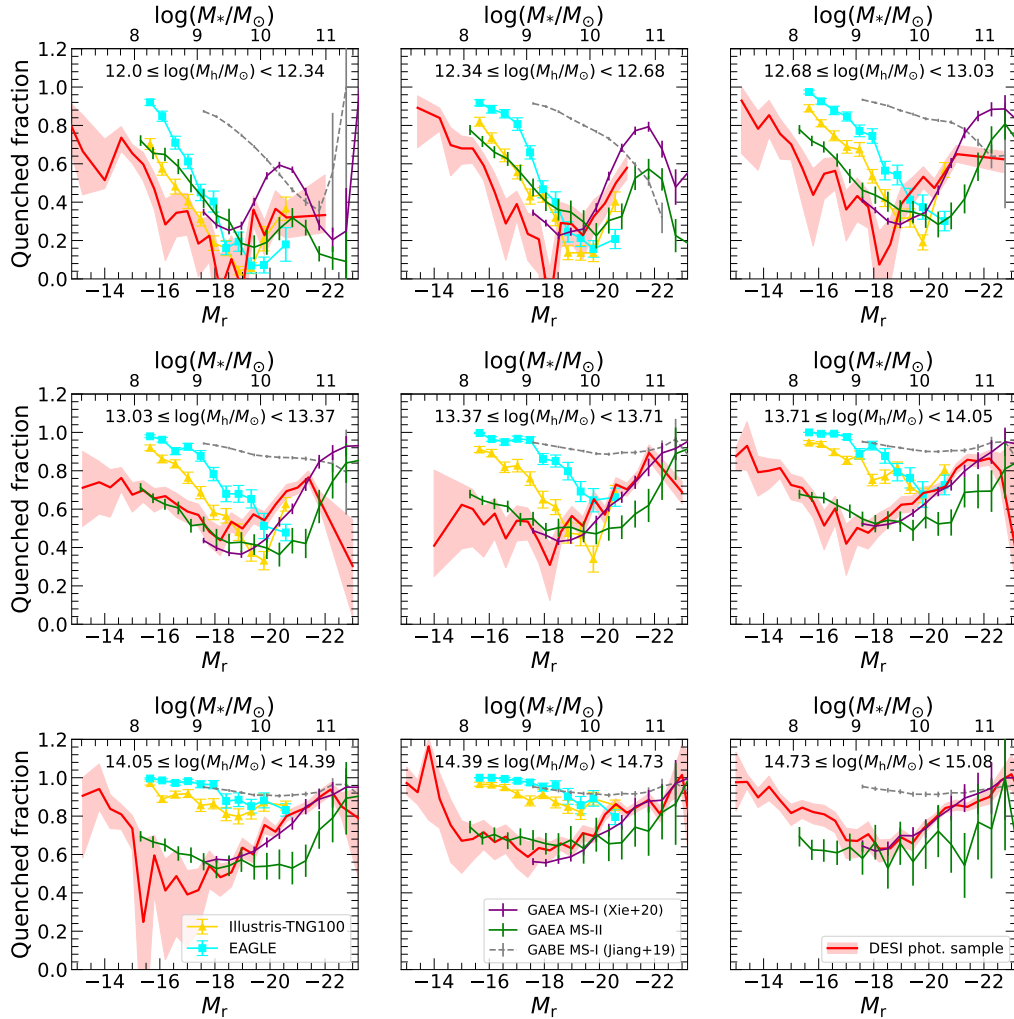


Figure 13. Our measurements of the old fraction in different halo mass intervals (indicated in each panel) are compared to the quenched fractions predicted by the GAEA semi-analytic model of Xie et al. (2020, purple line for result with the Millennium simulation and green line for that with the Millennium-II simulation), the GABE semi-analytic model of Jiang et al. (2019, grey dashed line), and the TNG (yellow triangles) and EAGLE (cyan squares) simulations.

processes for satellites in halos with low-to-intermediate mass and massive satellites in massive halos, but not for low-mass satellites in massive halos.

In the same figure, we also compare our result with the quenched fractions in two different semi-analytic models of galaxy formation: Galaxy Assembly with Binary Evolution (GABE; Jiang et al. 2019), and GALaxy Evolution and Assembly (GAEA; Hirschmann et al. 2016; Xie et al. 2017; De Lucia et al. 2019; Xie et al. 2020). The GABE model follows the same recipes of satellite quenching as in early models (e.g. Guo et al. 2011b), where the quenching of satellites occurs only by *starvation* or equivalently *strangulation* (Larson et al. 1980; Balogh & Morris 2000), with a gradual removal instead of instantaneous stripping of hot gas after they fall into their host halos. Consistent with what is previously known (e.g. Font et al. 2008; Guo et al. 2011b;

Hirschmann et al. 2014), Figure 13 shows that this model predicts too high a quenched fraction at all luminosities except at the bright end ($M_r \lesssim -21$, or $M_* \gtrsim 10^{11} M_\odot$), and this is true for all halo masses.

Xie et al. (2020) compared the fraction of quenched galaxies as a function of galaxy stellar mass down to $M_* \sim 10^9 M_\odot$ obtained from the SDSS by Wetzel et al. (2012) and Hirschmann et al. (2014) with those predicted by four semi-analytic models: L-Galaxies (Henriques et al. 2017), SAG (Cora et al. 2018), GAEA (Xie et al. 2017), and a modified version of the GAEA model by the authors themselves with improved treatments on environmental effects. All the models were found to reproduce the overall trends in the observational data (see Fig.9 of Xie et al. 2020). In Figure 13, the purple lines with (Poisson) error bars repeat the results of the modified GAEA code of Xie et al. (2020) ap-

plied to the Millennium Simulation (MS; Springel et al. 2005). Here we extend the predictions to a lower mass limit ($M_* \sim 10^8 M_\odot$) by applying the same code to the Millennium-II Simulation (MS-II; Boylan-Kolchin et al. 2009). As one can see, the GAEA model performs much better than GABE in matching our measurements at all halo masses, presumably because of the better treatment for satellite quenching. The differences in the model prediction between MS and MS-II are produced by the difference in numerical resolution, and by the fact that the model parameters were tuned only according to the MS. As pointed out in De Lucia et al. (2019) and Hirschmann et al. (2016), the success of GAEA is achieved not only by the improved treatment of satellite quenching (e.g. environmental effects considered in Xie et al. 2020), but more importantly by the large cold gas mass in satellites at the time of infall due to mechanisms implemented to regulate the gas-to-star conversion prior to infall, and by a lower rate implemented for gas heating by supernova explosions and stellar winds after the infall. We note that the same success is also achieved by the updated L-Galaxies model of Henriques et al. (2017) by using a more comprehensive treatment of satellite quenching.

As pointed out above, the old populations selected by $(g - z)$ in our case may still contain recent star formation, and they could be classified as star-forming if the quenched fraction is defined according to star formation rate. Therefore, the comparison results presented here should be taken with caution. A detailed comparison of the different models/simulations with our measurements, with the different definitions of quenched fraction being carefully taken into account, is needed to understand how our results can be used to constrain quenching processes quantitatively. This is beyond the scope of the present paper and we will come back to it in a forthcoming paper.

5. DISCUSSION

5.1. Implications of the characteristic mass

It is interesting to see how the characteristic luminosity at $M_r \sim -18$ ($M_* \sim 10^{9.5} M_\odot$) found here for member galaxies of clusters/groups compares to other observations along the same line. Traditionally, a B -band magnitude at -18 has been used to separate elliptical galaxies into dwarf and normal populations. These two populations seem to follow two distinct trends in the relation between surface brightness and absolute magnitude, with the dwarf population showing a much steeper increase of surface brightness with luminosity (Kormendy 1977, 1985; Graham & Guzmán 2003; Ferrarese et al. 2006; Kormendy et al. 2009). Using a large sample of SDSS galaxies, Shen et al. (2003) found that

red dwarf galaxies with $-16 < M_r < -18$ have similar sizes, while brighter red galaxies show a strong increase in size with luminosity (see their fig.13). These previous results suggest that there may be a dichotomy in structural properties between galaxies separated at $M_B \sim -18$. It is more meaningful to make the comparison in terms of stellar mass instead of luminosity in different bands. According to the empirical stellar mass estimators in Bell & de Jong (2001) and Bell et al. (2003), $M_B = -18$ corresponds to a stellar mass $M_* = 10^{9.1} \sim 10^{9.9} M_\odot$ for a typical color range of $B - R = 0.8 \sim 1.5$, consistent with the average mass of $M_* \sim 10^{9.5} M_\odot$ for galaxies with $M_r \sim -18$ in our sample. This implies that, for galaxies in groups/clusters, the dichotomy in the stellar population we find here and that in galaxy structure found in previous studies may be driven by some common processes that operate in groups/clusters of galaxies. For example, tidal stripping and galaxy interaction in dark matter halos may not only affect gas contents of satellite galaxies, but also have impacts on the stellar content and structure of galaxies. These effects are expected to be more effective for lower-mass (fainter) galaxies with lower surface densities (e.g. Li et al. 2012; Zhang et al. 2013). Analyses based on galaxy groups/clusters suggest that strangulation may be more important for quenching star formation in satellites more massive than $M_* \sim 10^{9.5} M_\odot$ (e.g. Weinmann et al. 2006a,b; van den Bosch et al. 2008; van der Wel et al. 2010; von der Linden et al. 2010). In the strangulation process, the hot gas halo around a galaxy is removed gradually, and so the quenching time scale associated with it is expected to be longer than that caused by the more violent processes, such as ram-pressure and tidal stripping. In a more recent study by Li et al. (2020) based on the SDSS groups, the quenched fraction of member galaxies of groups is found to exhibit a minimum, but at a characteristic mass scale that depends on both the central galaxy mass and the host halo mass. Quantitatively, their characteristic mass is comparable to ours only for Milky-Way size halos, i.e. at $M_* \sim 10^{9.5} M_\odot$; as halo mass increases, the stellar mass for the demarcation increases up to $M_* > 10^{10.5} M_\odot$ for the most massive halos with $M_h > 10^{14} M_\odot$ (see their fig.3). As pointed out by the authors, their results imply that galaxy quenching is not simply driven by the central-satellite dichotomy, but determined by the interaction between internal and environmental processes. Our results for faint satellites at $M_* < 10^{9.5} M_\odot$ combined with those obtained earlier for more massive galaxies seem to indicate that there are two characteristic mass scales, one is a fixed mass scale $M_1 \sim 10^{9.5} M_\odot$ found here, and the other one, M_2 , which depends on

halo mass as found in Li et al. (2020). For red galaxies at $M_* < M_1$ (which are predominately satellites), violent processes such as tidal and ram-pressure stripping may play the dominant role in quenching star formation, while for galaxies above M_1 , the quenching may be driven by a gradual removal of their hot halo gas through strangulation if $M_* < M_2$ or by internal processes, such as AGN feedback, if $M_* > M_2$.

5.2. The faint-end upturn and implications for galaxy formation at high redshift

The faint-end upturn in the luminosity function of galaxies in groups/clusters has long been in debate, as mentioned in Introduction. In the present paper, we have obtained the most reliable measurements of CLFs for groups with halo mass $M_h \gtrsim 10^{12} M_\odot$ and for galaxies down to $M_r = -10 \sim -12$, using a well-defined sample of central galaxies with halo mass information from the groups of Yang et al. (2007), the updated photometric sample of DESI, and the use of the $(g - z)$ color that is able to provide a more reliable separation between the old and young galaxy populations. Our results confirm the presence of a faint-end upturn for the red/old satellite population in halos of a wide range of mass, as shown in Figure 6. For the total CLFs, although the faint-end slope we obtain here, $\alpha \sim -1.6$, is somewhat steeper than that obtained earlier, it is actually comparable to that for field galaxies. For example, Blanton et al. (2005a) obtained $\alpha \sim -1.5$ after correcting for the incompleteness in the SDSS sample, and Li et al. (2022) obtained $\alpha \sim -1.6$ (see their figure 8) after correcting the cosmic variance effect in the SDSS sample (Chen et al. 2019). Recent measurements of galaxy stellar mass function (GSMF) in the GAMA sample showed that the faint-end slope is about $\alpha \sim -1.53$ (Driver et al. 2022), and that there is an upturn in the GSMF at $M_* \sim 10^{9.5} M_\odot$. Such an upturn may be produced by that seen in the CLF, particularly of red satellites. However, the GSMF obtained from the SDSS sample by Chen et al. (2019) shows an upturn mass that is slightly larger, at $M_* \sim 10^{10} M_\odot$. Since the upturn in the total GSMF of field galaxies is relatively weak, the feature may be more difficult to quantify. The faint-end upturn in the CLF is seen only for red/old satellites, with a slope of $\alpha \sim -1.8$ and a turnaround luminosity at $M_r \sim -18$, both of which are almost independent of halo mass (see Figure 7). The CLFs of blue satellites can be well described by a single Schechter function with a flatter slope of $\alpha \sim -1.25$, independent of halo mass. As shown by Figure 5 and Figure 6, it is the blue population that raises the amplitude of the luminosity function (LF) at $M_r < -18$, producing a total LF without a significant

upturn at the faint end, although the red/old population dominates the total abundance at the faint end. In the highest halo mass bin, which corresponds to the mass range of nearby rich clusters used in earlier studies, the total LF is dominated by the red population at almost all luminosities. This explains why the faint-end upturn was observed for those rich clusters in earlier studies. Controversial results in previous studies may be caused, at least partly, by the different fractions of the red/old population due to different photometric bands used to select satellite galaxies.

Although the origin of the faint-end slope of the total CLF, and in particular the upturn observed for red galaxies, are still poorly understood, it is clear that they contain important information about the formation and evolution of low-mass galaxies. For instance, in the empirical model developed by Lu et al. (2014) and Lu et al. (2015), a star formation burst at $z > 2$ was required for dwarf galaxies with $M_* \lesssim 10^9 M_\odot$ in order for their model to reproduce the faint-end upturn in the CLF of clusters obtained by Popesso et al. (2006). A natural prediction of this model is that the predicted mean stellar age of galaxies has a minimum at $\sim 10^{9.5} M_\odot$ (see their fig.14), which is consistent with our finding of the characteristic mass in the old fraction as a function of galaxy luminosity. Another prediction from the model of Lu et al. (2014) and Lu et al. (2015) is steep faint-end slopes of galaxy LFs at $z > 2$, which implies higher stellar mass (or luminosity) to dark matter mass ratios in low-mass halos as one goes to higher redshift (see fig.3 of Lu et al. 2015). The relation between galaxy luminosity/stellar mass and host halo mass has often been obtained from the abundance matching model, by matching the abundance of galaxies above a luminosity threshold with the abundance of subhalos with mass (defined at the time when the subhalo was accreted by its host halo) above a threshold. L16 extended the abundance matching model to relate the faint-end slope of CLFs (α) with the ‘‘efficiency’’ of star formation in low-mass halos using a parameterized form $L \propto m^\beta$, where L is galaxy luminosity and m is the un-evolved subhalo mass. Assuming that the number density is dominated by faint galaxies, i.e. $\alpha < -1$, this matching leads to a simple relation between α and β : $\beta \approx -0.8/(1 + \alpha)$. For blue satellites with $\alpha = -1.25$ from our CLFs, this relation implies that $L \propto m^3$, which is steeper than the relation of $L \propto m^{3/2}$ obtained by L16. The difference is caused by the significant faint end upturn in the CLFs of blue satellites obtained in L16 (see the comparison of CLFs in Figure 5). As demonstrated in subsection 3.4, a fraction of the blue galaxies identified by the $(u - r)$ color in L16 are actually red (and old) when classified

according to $(g-z)$, which may explain the discrepancy. For the red population, both L16 and our results give a faint-end slope of $\alpha \approx -1.8$, implying that $L \propto m$.

As suggested in L16, the different faint-end slopes, or equivalently the different $L-m$ relations, for the red and blue populations imply a dichotomy in the formation processes of the present-day galaxy population, with a characteristic redshift z_c at which the mode of star formation made a change. At $z > z_c$, the star formation efficiency (as measured by the stellar mass to halo mass ratio) in low-mass halos is roughly independent of halo mass, while at $z < z_c$ the efficiency increases rapidly with halo mass. For satellite galaxies, their star formation continues until they became satellites in larger systems. Thereafter the star formation might be quenched and their stellar mass would not change much. Thus, for the old population of satellite galaxies which formed most of their stars early, their stellar mass distribution should inherit that at the time of formation, hence the steep slope. In contrast, for the young population of satellites, which became satellites late and formed most of their stars in a mode similar to that of field galaxies, their stellar mass distribution should resemble that of present-day field galaxies, as is seen in our results. This scenario is similar to that expected from the pre-heating model of Mo & Mao (2002, 2004), where the transition from an early phase of efficient star formation to a later phase of reduced star formation efficiency is predicted to occur at a time when the intergalactic gas was heated significantly.

Environmental effects after a galaxy falls into its host halo may also produce the faint-end upturn in the red/old population, if these effects are to convert a fraction of satellites from the young population to the old in a systematic way. Quantitatively, to obtain the faint-end slope of -1.8 for the old population from a slope of -1.6 for the total population, the conversion fraction should scale with luminosity as $\propto L^{-0.2}$. Thus, the observed faint-end upturn may also be explained by environmental effects (nurture), instead of formation processes (nature). However, it is unclear how the vastly different environments, as represented by the large range of halo mass, can produce the same trend in the conversion and a single characteristic mass scale at $\sim 10^{9.5}M_\odot$.

This ‘nature and nurture’ degeneracy can be broken by observing the luminosity/stellar mass functions of low-mass galaxies at high z . If the steep slope originates from ‘nature’ (formation), then high- z galaxies, which are the progenitors of old galaxies observed in present-day clusters/groups, should be expected to have a steep luminosity/stellar mass function at the faint end. On the other hand, if the steep slope is produced by ‘nur-

ture’ (later environmental effects), then a steep slope is not expected for galaxies at high redshift. Observations of galaxy luminosity/stellar mass functions at high z down to a stellar mass below $\sim 10^{9.5}M_\odot$ are crucial to test the different scenarios. Recent observations based on ALMA (e.g. Gruppioni et al. 2020; Loiacono et al. 2021; Khusanova et al. 2021) found a much higher cosmic star formation rate density at $4 \lesssim z \lesssim 6$ than previously derived from UV-selected galaxies, suggesting that star formation may be more efficient at high z . More recent results from the Early Release Observations and Early Release Science Program of the JWST (e.g. Donnan et al. 2022; Harikane et al. 2022) also revealed a high cosmic density of star formation rate at high z . Clearly, with the advent of such observational data, we should be able to distinguish these different scenarios.

6. SUMMARY

In this paper, we use the DESI-DR9 imaging data down to the r -band magnitude limit of $r = 23$ and the group catalogue of galaxies from the SDSS spectroscopic survey to study the galaxy populations in groups/clusters with halo mass $M_h \geq 10^{12}M_\odot$ and redshift in the redshift range $0.01 \leq z \leq 0.08$. With central galaxies from the group catalog and satellites galaxies sampled with the imaging data, we measure the conditional luminosity functions (CLFs) in groups of different halo mass down to $M_r = -10 \sim -12$ mag, more than 2 magnitudes fainter than the limits achieved in previous investigations. We use the $(g-z)$ color to separate satellite galaxies into red and blue populations, and measure the CLFs separately for both. We calculate the fraction of the red population as a function of galaxy luminosity in halos of different mass, and use stellar population synthesis models to demonstrate the color bimodality of group galaxies is driven mainly by the stellar age of galaxies combined with the observed metallicity-mass relation. Our main results can be summarized as follows.

1. The CLFs we obtain are in good agreement with previous measurements, but with better statistics and down to fainter luminosities thanks to the much deeper imaging data from DESI-DR9.
2. We find clear bimodal distributions of group galaxies in $(g-z)$ color, which can be used to separate galaxies into red and blue modes that are cleaner than those from the widely-used $(u-r)$ color, particularly for faint galaxies.
3. Our CLF measurements of red and blue galaxies are broadly consistent with those obtained previously. We also find a clear upturn in the faint-

end of the CLFs for red galaxies, with a faint-end slope $\alpha \approx -1.8$, similar to the slope of the halo mass function at the low-mass end predicted by the current Λ CDM model.

4. Our results using stellar population synthesis models indicate that group galaxies in the red mode are dominated by old stellar populations, independent of galaxy luminosity (mass), although the red mode becomes bluer as luminosity decreases due to the change of metallicity with luminosity. Group galaxies in the blue mode also contain a large fraction of old stellar populations, but a more-or-less constant star formation extending to the recent past is needed to match their colors, particularly for low-luminosity galaxies.
5. The fraction of old galaxies as a function of galaxy luminosity has a minimum at a characteristic luminosity $M_r \sim -18$ independent of halo mass, which corresponds to a stellar mass scale of $M_* \sim 10^{9.5} M_\odot$. This luminosity/mass scale is comparable to the characteristic luminosity with which galaxies show a dichotomy in surface brightness. This suggests that the dichotomy in the old fraction found here for group/cluster galaxies and the dichotomy in galaxy structure found earlier may be driven by similar processes.
6. The rising of the old fraction at the faint end is consistent with the quenched fraction obtained for the Milky Way and M31 system and from the ELVES survey.
7. Current semi-analytic models of galaxy formation are able to reproduce the quenched fraction down to $M_* \sim 10^8 M_\odot$, while both the Illustris-TNG and EAGLE simulations over-predict the quenched fraction of low-mass satellites ($M_* \lesssim 10^{10} M_\odot$) in halos more massive than the Milky Way halo mass.
8. Our results provide important information about the formation and quenching of satellite galaxies. The observed upturn in the number of old galaxies in the faint end, which suggests that the stellar masses in these galaxies are proportional to their halo masses, indicates that star formation and feedback efficiencies are independent of halo mass during the formation of these galaxies. This implies that the faint-end slope of the luminosity/stellar mass function of high- z galaxies is steep with $\alpha \sim -1.8$, a prediction that can be tested by JWST observations of low-mass galaxies ($M_* < 10^{9.5} M_\odot$) at high z . The presence of a

well-defined characteristic mass at $M_* \sim 10^{9.5} M_\odot$ in the old population fraction of satellites in halos of all masses indicates that the quenching of star formation is closely related to the formation and properties of galaxies, rather than their current environments.

ACKNOWLEDGMENTS

This work is supported by the National Key R&D Program of China (grant No. 2018YFA0404502), and the National Science Foundation of China (grant Nos. 11821303, 11733002, 11973030, 11673015, 11733004, 11761131004, 11761141012). The authors acknowledge the Tsinghua Astrophysics High-Performance Computing platform at Tsinghua University for providing computational and data storage resources that have contributed to the research results reported within this paper.

Funding for the SDSS and SDSS-II has been provided by the Alfred P. Sloan Foundation, the Participating Institutions, the National Science Foundation, the U.S. Department of Energy, the National Aeronautics and Space Administration, the Japanese Monbukagakusho, the Max Planck Society, and the Higher Education Funding Council for England. The SDSS Web Site is <http://www.sdss.org/>.

The SDSS is managed by the Astrophysical Research Consortium for the Participating Institutions. The Participating Institutions are the American Museum of Natural History, Astrophysical Institute Potsdam, University of Basel, University of Cambridge, Case Western Reserve University, University of Chicago, Drexel University, Fermilab, the Institute for Advanced Study, the Japan Participation Group, Johns Hopkins University, the Joint Institute for Nuclear Astrophysics, the Kavli Institute for Particle Astrophysics and Cosmology, the Korean Scientist Group, the Chinese Academy of Sciences (LAMOST), Los Alamos National Laboratory, the Max-Planck-Institute for Astronomy (MPIA), the Max-Planck-Institute for Astrophysics (MPA), New Mexico State University, Ohio State University, University of Pittsburgh, University of Portsmouth, Princeton University, the United States Naval Observatory, and the University of Washington.

The Legacy Surveys consist of three individual and complementary projects: the Dark Energy Camera Legacy Survey (DECaLS; Proposal ID #2014B-0404; PIs: David Schlegel and Arjun Dey), the Beijing-Arizona Sky Survey (BASS; NOAO Prop. ID #2015A-0801; PIs: Zhou Xu and Xiaohui Fan), and the Mayall z -band Legacy Survey (MzLS; Prop. ID #2016A-0453; PI: Arjun Dey). DECaLS, BASS and MzLS together

include data obtained, respectively, at the Blanco telescope, Cerro Tololo Inter-American Observatory, NSF’s NOIRLab; the Bok telescope, Steward Observatory, University of Arizona; and the Mayall telescope, Kitt Peak National Observatory, NOIRLab. Pipeline processing and analyses of the data were supported by NOIRLab and the Lawrence Berkeley National Laboratory (LBNL). The Legacy Surveys project is honored to be permitted to conduct astronomical research on Iolkam Du’ag (Kitt Peak), a mountain with particular significance to the Tohono O’odham Nation.

NOIRLab is operated by the Association of Universities for Research in Astronomy (AURA) under a cooperative agreement with the National Science Foundation. LBNL is managed by the Regents of the University of California under contract to the U.S. Department of Energy.

This project used data obtained with the Dark Energy Camera (DECam), which was constructed by the Dark Energy Survey (DES) collaboration. Funding for the DES Projects has been provided by the U.S. Department of Energy, the U.S. National Science Foundation, the Ministry of Science and Education of Spain, the Science and Technology Facilities Council of the United Kingdom, the Higher Education Funding Council for England, the National Center for Supercomputing Applications at the University of Illinois at Urbana-Champaign, the Kavli Institute of Cosmological Physics at the University of Chicago, Center for Cosmology and Astro-Particle Physics at the Ohio State University, the Mitchell Institute for Fundamental Physics and Astronomy at Texas A&M University, Financiadora de Estudos e Projetos, Fundacao Carlos Chagas Filho de Amparo, Financiadora de Estudos e Projetos, Fundacao Carlos Chagas Filho de Amparo a Pesquisa do Estado do Rio de Janeiro, Conselho Nacional de Desenvolvimento Cientifico e Tecnologico and the Ministerio da Ciencia, Tecnologia e Inovacao, the Deutsche Forschungsgemeinschaft and the Collaborating Institutions in the Dark Energy Survey. The Collaborating Institutions are Argonne National Laboratory, the University of California at Santa Cruz, the University of Cambridge, Centro de Investigaciones Energeticas, Medioambientales y Tecnologicas-Madrid, the Univer-

sity of Chicago, University College London, the DES-Brazil Consortium, the University of Edinburgh, the Eidgenossische Technische Hochschule (ETH) Zurich, Fermi National Accelerator Laboratory, the University of Illinois at Urbana-Champaign, the Institut de Ciencies de l’Espai (IEEC/CSIC), the Institut de Fisica d’Altes Energies, Lawrence Berkeley National Laboratory, the Ludwig Maximilians Universitat Munchen and the associated Excellence Cluster Universe, the University of Michigan, NSF’s NOIRLab, the University of Nottingham, the Ohio State University, the University of Pennsylvania, the University of Portsmouth, SLAC National Accelerator Laboratory, Stanford University, the University of Sussex, and Texas A&M University.

BASS is a key project of the Telescope Access Program (TAP), which has been funded by the National Astronomical Observatories of China, the Chinese Academy of Sciences (the Strategic Priority Research Program “The Emergence of Cosmological Structures” Grant # XDB09000000), and the Special Fund for Astronomy from the Ministry of Finance. The BASS is also supported by the External Cooperation Program of Chinese Academy of Sciences (Grant # 114A11KYSB20160057), and Chinese National Natural Science Foundation (Grant # 12120101003, # 11433005).

The Legacy Survey team makes use of data products from the Near-Earth Object Wide-field Infrared Survey Explorer (NEOWISE), which is a project of the Jet Propulsion Laboratory/California Institute of Technology. NEOWISE is funded by the National Aeronautics and Space Administration.

The Legacy Surveys imaging of the DESI footprint is supported by the Director, Office of Science, Office of High Energy Physics of the U.S. Department of Energy under Contract No. DE-AC02-05CH1123, by the National Energy Research Scientific Computing Center, a DOE Office of Science User Facility under the same contract; and by the U.S. National Science Foundation, Division of Astronomical Sciences under Contract No. AST-0950945 to NOAO.

Software: Astropy (Astropy Collaboration et al. 2013, 2018), NumPy (Harris et al. 2020), SciPy (Virtanen et al. 2020), Matplotlib (Hunter 2007), h5py (Collette et al. 2021), emcee (Foreman-Mackey et al. 2013)

REFERENCES

- Abazajian, K. N., Adelman-McCarthy, J. K., Agüeros, M. A., et al. 2009, *ApJS*, 182, 543, doi: [10.1088/0067-0049/182/2/543](https://doi.org/10.1088/0067-0049/182/2/543)
- Agulli, I., Aguerri, J. A. L., Sanchez-Janssen, R., et al. 2014, *MNRAS*, 444, L34, doi: [10.1093/mnras/lu108](https://doi.org/10.1093/mnras/lu108)
- Ahumada, R., Prieto, C. A., Almeida, A., et al. 2020, *ApJS*, 249, 3, doi: [10.3847/1538-4365/ab929e](https://doi.org/10.3847/1538-4365/ab929e)

- Astropy Collaboration, Robitaille, T. P., Tollerud, E. J., et al. 2013, *A&A*, 558, A33, doi: [10.1051/0004-6361/201322068](https://doi.org/10.1051/0004-6361/201322068)
- Astropy Collaboration, Price-Whelan, A. M., Sipőcz, B. M., et al. 2018, *AJ*, 156, 123, doi: [10.3847/1538-3881/aabc4f](https://doi.org/10.3847/1538-3881/aabc4f)
- Bañados, E., Hung, L.-W., De Propris, R., & West, M. J. 2010, *ApJL*, 721, L14, doi: [10.1088/2041-8205/721/1/L14](https://doi.org/10.1088/2041-8205/721/1/L14)
- Baldry, I. K., Glazebrook, K., Brinkmann, J., et al. 2004, *ApJ*, 600, 681, doi: [10.1086/380092](https://doi.org/10.1086/380092)
- Balogh, M. L., & Morris, S. L. 2000, *MNRAS*, 318, 703, doi: [10.1046/j.1365-8711.2000.03826.x](https://doi.org/10.1046/j.1365-8711.2000.03826.x)
- Barkhouse, W. A., Yee, H. K. C., & López-Cruz, O. 2007, *ApJ*, 671, 1471, doi: [10.1086/523257](https://doi.org/10.1086/523257)
- . 2009, *ApJ*, 703, 2024, doi: [10.1088/0004-637X/703/2/2024](https://doi.org/10.1088/0004-637X/703/2/2024)
- Bell, E. F., & de Jong, R. S. 2001, *ApJ*, 550, 212, doi: [10.1086/319728](https://doi.org/10.1086/319728)
- Bell, E. F., McIntosh, D. H., Katz, N., & Weinberg, M. D. 2003, *ApJS*, 149, 289, doi: [10.1086/378847](https://doi.org/10.1086/378847)
- Bernstein, G. M., Nichol, R. C., Tyson, J. A., Ulmer, M. P., & Wittman, D. 1995, *AJ*, 110, 1507, doi: [10.1086/117624](https://doi.org/10.1086/117624)
- Binggeli, B., Sandage, A., & Tammann, G. A. 1988, *ARA&A*, 26, 509, doi: [10.1146/annurev.aa.26.090188.002453](https://doi.org/10.1146/annurev.aa.26.090188.002453)
- Blanton, M. R., Kazin, E., Muna, D., Weaver, B. A., & Price-Whelan, A. 2011, *AJ*, 142, 31, doi: [10.1088/0004-6256/142/1/31](https://doi.org/10.1088/0004-6256/142/1/31)
- Blanton, M. R., Lupton, R. H., Schlegel, D. J., et al. 2005a, *ApJ*, 631, 208, doi: [10.1086/431416](https://doi.org/10.1086/431416)
- Blanton, M. R., & Roweis, S. 2007, *AJ*, 133, 734, doi: [10.1086/510127](https://doi.org/10.1086/510127)
- Blanton, M. R., Schlegel, D. J., Strauss, M. A., et al. 2005b, *AJ*, 129, 2562, doi: [10.1086/429803](https://doi.org/10.1086/429803)
- Boselli, A., & Gavazzi, G. 2014, *A&A Rv*, 22, 74, doi: [10.1007/s00159-014-0074-y](https://doi.org/10.1007/s00159-014-0074-y)
- Boylan-Kolchin, M., Springel, V., White, S. D. M., Jenkins, A., & Lemson, G. 2009, *MNRAS*, 398, 1150, doi: [10.1111/j.1365-2966.2009.15191.x](https://doi.org/10.1111/j.1365-2966.2009.15191.x)
- Bruzual, G., & Charlot, S. 2003, *MNRAS*, 344, 1000, doi: [10.1046/j.1365-8711.2003.06897.x](https://doi.org/10.1046/j.1365-8711.2003.06897.x)
- Carlsten, S. G., Greene, J. E., Beaton, R. L., Danieli, S., & Greco, J. P. 2022, *ApJ*, 933, 47, doi: [10.3847/1538-4357/ac6fd7](https://doi.org/10.3847/1538-4357/ac6fd7)
- Chabrier, G. 2003, *PASP*, 115, 763, doi: [10.1086/376392](https://doi.org/10.1086/376392)
- Chen, Y., Mo, H. J., Li, C., et al. 2019, *ApJ*, 872, 180, doi: [10.3847/1538-4357/ab0208](https://doi.org/10.3847/1538-4357/ab0208)
- Colless, M., Dalton, G., Maddox, S., et al. 2001, *MNRAS*, 328, 1039, doi: [10.1046/j.1365-8711.2001.04902.x](https://doi.org/10.1046/j.1365-8711.2001.04902.x)
- Collette, A., Kluyver, T., Caswell, T. A., et al. 2021, *h5py/h5py*: 3.5.0, 3.5.0, Zenodo, Zenodo, doi: [10.5281/zenodo.5585380](https://doi.org/10.5281/zenodo.5585380)
- Cooray, A. 2006, *MNRAS*, 365, 842, doi: [10.1111/j.1365-2966.2005.09747.x](https://doi.org/10.1111/j.1365-2966.2005.09747.x)
- Cora, S. A., Vega-Martínez, C. A., Hough, T., et al. 2018, *MNRAS*, 479, 2, doi: [10.1093/mnras/sty1131](https://doi.org/10.1093/mnras/sty1131)
- Crain, R. A., Schaye, J., Bower, R. G., et al. 2015, *MNRAS*, 450, 1937, doi: [10.1093/mnras/stv725](https://doi.org/10.1093/mnras/stv725)
- de Filippis, E., Paolillo, M., Longo, G., et al. 2011, *MNRAS*, 414, 2771, doi: [10.1111/j.1365-2966.2011.18596.x](https://doi.org/10.1111/j.1365-2966.2011.18596.x)
- De Lucia, G., Hirschmann, M., & Fontanot, F. 2019, *MNRAS*, 482, 5041, doi: [10.1093/mnras/sty3059](https://doi.org/10.1093/mnras/sty3059)
- de Propris, R., Pritchet, C. J., Harris, W. E., & McClure, R. D. 1995, *ApJ*, 450, 534, doi: [10.1086/176163](https://doi.org/10.1086/176163)
- Dey, A., Schlegel, D. J., Lang, D., et al. 2019, *AJ*, 157, 168, doi: [10.3847/1538-3881/ab089d](https://doi.org/10.3847/1538-3881/ab089d)
- Donnan, C. T., McLeod, D. J., Dunlop, J. S., et al. 2022, *arXiv e-prints*, arXiv:2207.12356, <https://arxiv.org/abs/2207.12356>
- Driver, S. P., Odewahn, S. C., Echevarria, L., et al. 2003, *AJ*, 126, 2662, doi: [10.1086/379560](https://doi.org/10.1086/379560)
- Driver, S. P., Phillipps, S., Davies, J. I., Morgan, I., & Disney, M. J. 1994, *MNRAS*, 268, 393, doi: [10.1093/mnras/268.2.393](https://doi.org/10.1093/mnras/268.2.393)
- Driver, S. P., Bellstedt, S., Robotham, A. S. G., et al. 2022, *MNRAS*, 513, 439, doi: [10.1093/mnras/stac472](https://doi.org/10.1093/mnras/stac472)
- Ferrarese, L., Côté, P., Jordán, A., et al. 2006, *ApJS*, 164, 334, doi: [10.1086/501350](https://doi.org/10.1086/501350)
- Ferrarese, L., Côté, P., Sánchez-Janssen, R., et al. 2016, *ApJ*, 824, 10, doi: [10.3847/0004-637X/824/1/10](https://doi.org/10.3847/0004-637X/824/1/10)
- Font, A. S., Bower, R. G., McCarthy, I. G., et al. 2008, *MNRAS*, 389, 1619, doi: [10.1111/j.1365-2966.2008.13698.x](https://doi.org/10.1111/j.1365-2966.2008.13698.x)
- Foreman-Mackey, D., Hogg, D. W., Lang, D., & Goodman, J. 2013, *PASP*, 125, 306, doi: [10.1086/670067](https://doi.org/10.1086/670067)
- Geha, M., Blanton, M. R., Yan, R., & Tinker, J. L. 2012, *ApJ*, 757, 85, doi: [10.1088/0004-637X/757/1/85](https://doi.org/10.1088/0004-637X/757/1/85)
- Geha, M., Wechsler, R. H., Mao, Y.-Y., et al. 2017, *ApJ*, 847, 4, doi: [10.3847/1538-4357/aa8626](https://doi.org/10.3847/1538-4357/aa8626)
- Gibson, B. K., & Matteucci, F. 1997, *ApJ*, 475, 47, doi: [10.1086/303513](https://doi.org/10.1086/303513)
- Graham, A. W., & Guzmán, R. 2003, *AJ*, 125, 2936, doi: [10.1086/374992](https://doi.org/10.1086/374992)
- Gruppioni, C., Béthermin, M., Loiacono, F., et al. 2020, *A&A*, 643, A8, doi: [10.1051/0004-6361/202038487](https://doi.org/10.1051/0004-6361/202038487)
- Guo, H., Yang, X., & Lu, Y. 2018, *ApJ*, 858, 30, doi: [10.3847/1538-4357/aabc56](https://doi.org/10.3847/1538-4357/aabc56)
- Guo, Q., Cole, S., Eke, V., & Frenk, C. 2011a, *MNRAS*, 417, 370, doi: [10.1111/j.1365-2966.2011.19270.x](https://doi.org/10.1111/j.1365-2966.2011.19270.x)

- Guo, Q., White, S., Boylan-Kolchin, M., et al. 2011b, *MNRAS*, 413, 101, doi: [10.1111/j.1365-2966.2010.18114.x](https://doi.org/10.1111/j.1365-2966.2010.18114.x)
- Hansen, S. M., McKay, T. A., Wechsler, R. H., et al. 2005, *ApJ*, 633, 122, doi: [10.1086/444554](https://doi.org/10.1086/444554)
- Hansen, S. M., Sheldon, E. S., Wechsler, R. H., & Koester, B. P. 2009, *ApJ*, 699, 1333, doi: [10.1088/0004-637X/699/2/1333](https://doi.org/10.1088/0004-637X/699/2/1333)
- Harikane, Y., Ouchi, M., Oguri, M., et al. 2022, arXiv e-prints, arXiv:2208.01612, <https://arxiv.org/abs/2208.01612>
- Harris, C. R., Millman, K. J., van der Walt, S. J., et al. 2020, *Nature*, 585, 357, doi: [10.1038/s41586-020-2649-2](https://doi.org/10.1038/s41586-020-2649-2)
- Harsono, D., & De Propriis, R. 2009, *AJ*, 137, 3091, doi: [10.1088/0004-6256/137/2/3091](https://doi.org/10.1088/0004-6256/137/2/3091)
- Hashimoto, Y., Böhringer, H., & Umetsu, K. 2022, *MNRAS*, 511, 2796, doi: [10.1093/mnras/stac209](https://doi.org/10.1093/mnras/stac209)
- Henriques, B. M. B., White, S. D. M., Thomas, P. A., et al. 2017, *MNRAS*, 469, 2626, doi: [10.1093/mnras/stx1010](https://doi.org/10.1093/mnras/stx1010)
- Hirschmann, M., De Lucia, G., & Fontanot, F. 2016, *MNRAS*, 461, 1760, doi: [10.1093/mnras/stw1318](https://doi.org/10.1093/mnras/stw1318)
- Hirschmann, M., De Lucia, G., Wilman, D., et al. 2014, *MNRAS*, 444, 2938, doi: [10.1093/mnras/stu1609](https://doi.org/10.1093/mnras/stu1609)
- Huang, J. S., Cowie, L. L., Gardner, J. P., et al. 1997, *ApJ*, 476, 12, doi: [10.1086/303598](https://doi.org/10.1086/303598)
- Hunter, J. D. 2007, *Computing in Science & Engineering*, 9, 90, doi: [10.1109/MCSE.2007.55](https://doi.org/10.1109/MCSE.2007.55)
- Jiang, Z., Wang, J., Gao, L., et al. 2019, *Research in Astronomy and Astrophysics*, 19, 151, doi: [10.1088/1674-4527/19/10/151](https://doi.org/10.1088/1674-4527/19/10/151)
- Karunakaran, A., Sand, D. J., Jones, M. G., et al. 2022, arXiv e-prints, arXiv:2210.03748, <https://arxiv.org/abs/2210.03748>
- Kashibadze, O. G., Karachentsev, I. D., & Karachentseva, V. E. 2020, *A&A*, 635, A135, doi: [10.1051/0004-6361/201936172](https://doi.org/10.1051/0004-6361/201936172)
- Khusanova, Y., Bethermin, M., Le Fèvre, O., et al. 2021, *A&A*, 649, A152, doi: [10.1051/0004-6361/202038944](https://doi.org/10.1051/0004-6361/202038944)
- Kirby, E. N., Cohen, J. G., Guhathakurta, P., et al. 2013, *ApJ*, 779, 102, doi: [10.1088/0004-637X/779/2/102](https://doi.org/10.1088/0004-637X/779/2/102)
- Komatsu, E., Smith, K. M., Dunkley, J., et al. 2011, *ApJS*, 192, 18, doi: [10.1088/0067-0049/192/2/18](https://doi.org/10.1088/0067-0049/192/2/18)
- Kormendy, J. 1977, *ApJ*, 217, 406, doi: [10.1086/155589](https://doi.org/10.1086/155589)
- . 1985, *ApJ*, 295, 73, doi: [10.1086/163350](https://doi.org/10.1086/163350)
- Kormendy, J., Fisher, D. B., Cornell, M. E., & Bender, R. 2009, *ApJS*, 182, 216, doi: [10.1088/0067-0049/182/1/216](https://doi.org/10.1088/0067-0049/182/1/216)
- Kubo, J. M., Stebbins, A., Annis, J., et al. 2007, *ApJ*, 671, 1466, doi: [10.1086/523101](https://doi.org/10.1086/523101)
- Lan, T.-W., Ménard, B., & Mo, H. 2016, *MNRAS*, 459, 3998, doi: [10.1093/mnras/stw898](https://doi.org/10.1093/mnras/stw898)
- Larson, R. B., Tinsley, B. M., & Caldwell, C. N. 1980, *ApJ*, 237, 692, doi: [10.1086/157917](https://doi.org/10.1086/157917)
- Lee, Y., Rey, S.-C., Hilker, M., Sheen, Y.-K., & Yi, S. K. 2016, *ApJ*, 822, 92, doi: [10.3847/0004-637X/822/2/92](https://doi.org/10.3847/0004-637X/822/2/92)
- Li, C., Kauffmann, G., Fu, J., et al. 2012, *MNRAS*, 424, 1471, doi: [10.1111/j.1365-2966.2012.21337.x](https://doi.org/10.1111/j.1365-2966.2012.21337.x)
- Li, P., Wang, H., Mo, H. J., Wang, E., & Hong, H. 2020, *ApJ*, 902, 75, doi: [10.3847/1538-4357/abb66c](https://doi.org/10.3847/1538-4357/abb66c)
- Li, X., Li, C., Mo, H. J., Xiao, T., & Wang, J. 2022, arXiv e-prints, arXiv:2209.07691, <https://arxiv.org/abs/2209.07691>
- Lieder, S., Lisker, T., Hilker, M., Misgeld, I., & Durrell, P. 2012, *A&A*, 538, A69, doi: [10.1051/0004-6361/201117163](https://doi.org/10.1051/0004-6361/201117163)
- Loiacono, F., Decarli, R., Gruppioni, C., et al. 2021, *A&A*, 646, A76, doi: [10.1051/0004-6361/202038607](https://doi.org/10.1051/0004-6361/202038607)
- Lu, Z., Mo, H. J., Lu, Y., et al. 2014, *MNRAS*, 439, 1294, doi: [10.1093/mnras/stu016](https://doi.org/10.1093/mnras/stu016)
- . 2015, *MNRAS*, 450, 1604, doi: [10.1093/mnras/stv667](https://doi.org/10.1093/mnras/stv667)
- Mao, Y.-Y., Geha, M., Wechsler, R. H., et al. 2021, *ApJ*, 907, 85, doi: [10.3847/1538-4357/abce58](https://doi.org/10.3847/1538-4357/abce58)
- McAlpine, S., Helly, J. C., Schaller, M., et al. 2016, *Astronomy and Computing*, 15, 72, doi: [10.1016/j.ascom.2016.02.004](https://doi.org/10.1016/j.ascom.2016.02.004)
- Meusinger, H., Rudolf, C., Stecklum, B., et al. 2020, *A&A*, 640, A30, doi: [10.1051/0004-6361/202037574](https://doi.org/10.1051/0004-6361/202037574)
- Misgeld, I., Hilker, M., & Mieske, S. 2009, *A&A*, 496, 683, doi: [10.1051/0004-6361/200811451](https://doi.org/10.1051/0004-6361/200811451)
- Misgeld, I., Mieske, S., & Hilker, M. 2008, *A&A*, 486, 697, doi: [10.1051/0004-6361:200810014](https://doi.org/10.1051/0004-6361:200810014)
- Mo, H., van den Bosch, F. C., & White, S. 2010, *Galaxy Formation and Evolution*
- Mo, H. J., & Mao, S. 2002, *MNRAS*, 333, 768, doi: [10.1046/j.1365-8711.2002.05416.x](https://doi.org/10.1046/j.1365-8711.2002.05416.x)
- . 2004, *MNRAS*, 353, 829, doi: [10.1111/j.1365-2966.2004.08114.x](https://doi.org/10.1111/j.1365-2966.2004.08114.x)
- Mobasher, B., Colless, M., Carter, D., et al. 2003, *ApJ*, 587, 605, doi: [10.1086/368305](https://doi.org/10.1086/368305)
- Nelson, D., Springel, V., Pillepich, A., et al. 2019, *Computational Astrophysics and Cosmology*, 6, 2, doi: [10.1186/s40668-019-0028-x](https://doi.org/10.1186/s40668-019-0028-x)
- Parolin, I., Molinari, E., & Chincarini, G. 2003, *A&A*, 407, 823, doi: [10.1051/0004-6361:20030900](https://doi.org/10.1051/0004-6361:20030900)
- Pillepich, A., Nelson, D., Hernquist, L., et al. 2018, *MNRAS*, 475, 648, doi: [10.1093/mnras/stx3112](https://doi.org/10.1093/mnras/stx3112)
- Popesso, P., Biviano, A., Böhringer, H., & Romaniello, M. 2006, *A&A*, 445, 29, doi: [10.1051/0004-6361:20052954](https://doi.org/10.1051/0004-6361:20052954)
- Popesso, P., Böhringer, H., Romaniello, M., & Voges, W. 2005, *A&A*, 433, 415, doi: [10.1051/0004-6361:20041870](https://doi.org/10.1051/0004-6361:20041870)

- Pracy, M. B., De Propriis, R., Driver, S. P., Couch, W. J., & Nulsen, P. E. J. 2004, *MNRAS*, 352, 1135, doi: [10.1111/j.1365-2966.2004.08008.x](https://doi.org/10.1111/j.1365-2966.2004.08008.x)
- Rines, K., & Geller, M. J. 2008, *AJ*, 135, 1837, doi: [10.1088/0004-6256/135/5/1837](https://doi.org/10.1088/0004-6256/135/5/1837)
- Robotham, A., Phillipps, S., & de Propriis, R. 2010, *MNRAS*, 403, 1812, doi: [10.1111/j.1365-2966.2010.16252.x](https://doi.org/10.1111/j.1365-2966.2010.16252.x)
- Sales, L. V., Wang, W., White, S. D. M., & Navarro, J. F. 2013, *MNRAS*, 428, 573, doi: [10.1093/mnras/sts054](https://doi.org/10.1093/mnras/sts054)
- Schaye, J., Crain, R. A., Bower, R. G., et al. 2015, *MNRAS*, 446, 521, doi: [10.1093/mnras/stu2058](https://doi.org/10.1093/mnras/stu2058)
- Shen, S., Mo, H. J., White, S. D. M., et al. 2003, *MNRAS*, 343, 978, doi: [10.1046/j.1365-8711.2003.06740.x](https://doi.org/10.1046/j.1365-8711.2003.06740.x)
- Springel, V., White, S. D. M., Jenkins, A., et al. 2005, *Nature*, 435, 629, doi: [10.1038/nature03597](https://doi.org/10.1038/nature03597)
- Tinker, J. L., Cao, J., Alpaslan, M., et al. 2021, *MNRAS*, 505, 5370, doi: [10.1093/mnras/stab1576](https://doi.org/10.1093/mnras/stab1576)
- Trentham, N. 1994, *Nature*, 372, 157, doi: [10.1038/372157a0](https://doi.org/10.1038/372157a0)
- van den Bosch, F. C., Aquino, D., Yang, X., et al. 2008, *MNRAS*, 387, 79, doi: [10.1111/j.1365-2966.2008.13230.x](https://doi.org/10.1111/j.1365-2966.2008.13230.x)
- van den Bosch, F. C., Yang, X., & Mo, H. J. 2003, *MNRAS*, 340, 771, doi: [10.1046/j.1365-8711.2003.06335.x](https://doi.org/10.1046/j.1365-8711.2003.06335.x)
- van den Bosch, F. C., Yang, X., Mo, H. J., et al. 2007, *MNRAS*, 376, 841, doi: [10.1111/j.1365-2966.2007.11493.x](https://doi.org/10.1111/j.1365-2966.2007.11493.x)
- van der Wel, A., Bell, E. F., Holden, B. P., Skibba, R. A., & Rix, H.-W. 2010, *ApJ*, 714, 1779, doi: [10.1088/0004-637X/714/2/1779](https://doi.org/10.1088/0004-637X/714/2/1779)
- Vázquez-Mata, J. A., Loveday, J., Riggs, S. D., et al. 2020, *MNRAS*, 499, 631, doi: [10.1093/mnras/staa2889](https://doi.org/10.1093/mnras/staa2889)
- Virtanen, P., Gommers, R., Oliphant, T. E., et al. 2020, *Nature Methods*, 17, 261, doi: [10.1038/s41592-019-0686-2](https://doi.org/10.1038/s41592-019-0686-2)
- von der Linden, A., Wild, V., Kauffmann, G., White, S. D. M., & Weinmann, S. 2010, *MNRAS*, 404, 1231, doi: [10.1111/j.1365-2966.2010.16375.x](https://doi.org/10.1111/j.1365-2966.2010.16375.x)
- Wang, W., & White, S. D. M. 2012, *MNRAS*, 424, 2574, doi: [10.1111/j.1365-2966.2012.21256.x](https://doi.org/10.1111/j.1365-2966.2012.21256.x)
- Wang, W., Takada, M., Li, X., et al. 2021, *MNRAS*, 500, 3776, doi: [10.1093/mnras/staa3495](https://doi.org/10.1093/mnras/staa3495)
- Wechsler, R. H., & Tinker, J. L. 2018, *ARA&A*, 56, 435, doi: [10.1146/annurev-astro-081817-051756](https://doi.org/10.1146/annurev-astro-081817-051756)
- Weinmann, S. M., Lisker, T., Guo, Q., Meyer, H. T., & Janz, J. 2011, *MNRAS*, 416, 1197, doi: [10.1111/j.1365-2966.2011.19118.x](https://doi.org/10.1111/j.1365-2966.2011.19118.x)
- Weinmann, S. M., van den Bosch, F. C., Yang, X., & Mo, H. J. 2006a, *MNRAS*, 366, 2, doi: [10.1111/j.1365-2966.2005.09865.x](https://doi.org/10.1111/j.1365-2966.2005.09865.x)
- Weinmann, S. M., van den Bosch, F. C., Yang, X., et al. 2006b, *MNRAS*, 372, 1161, doi: [10.1111/j.1365-2966.2006.10932.x](https://doi.org/10.1111/j.1365-2966.2006.10932.x)
- Weisz, D. R., Dalcanton, J. J., Williams, B. F., et al. 2011, *ApJ*, 739, 5, doi: [10.1088/0004-637X/739/1/5](https://doi.org/10.1088/0004-637X/739/1/5)
- Wetzell, A. R., Tinker, J. L., & Conroy, C. 2012, *MNRAS*, 424, 232, doi: [10.1111/j.1365-2966.2012.21188.x](https://doi.org/10.1111/j.1365-2966.2012.21188.x)
- Wetzell, A. R., Tollerud, E. J., & Weisz, D. R. 2015, *ApJL*, 808, L27, doi: [10.1088/2041-8205/808/1/L27](https://doi.org/10.1088/2041-8205/808/1/L27)
- White, S. D. M., & Rees, M. J. 1978, *MNRAS*, 183, 341, doi: [10.1093/mnras/183.3.341](https://doi.org/10.1093/mnras/183.3.341)
- Xie, L., De Lucia, G., Hirschmann, M., & Fontanot, F. 2020, *MNRAS*, 498, 4327, doi: [10.1093/mnras/staa2370](https://doi.org/10.1093/mnras/staa2370)
- Xie, L., De Lucia, G., Hirschmann, M., Fontanot, F., & Zoldan, A. 2017, *MNRAS*, 469, 968, doi: [10.1093/mnras/stx889](https://doi.org/10.1093/mnras/stx889)
- Yagi, M., Kashikawa, N., Sekiguchi, M., et al. 2002, *AJ*, 123, 87, doi: [10.1086/324732](https://doi.org/10.1086/324732)
- Yamanoi, H., Tanaka, M., Hamabe, M., et al. 2007, *AJ*, 134, 56, doi: [10.1086/518475](https://doi.org/10.1086/518475)
- Yamanoi, H., Komiyama, Y., Yagi, M., et al. 2012, *AJ*, 144, 40, doi: [10.1088/0004-6256/144/2/40](https://doi.org/10.1088/0004-6256/144/2/40)
- Yang, X., Mo, H. J., & van den Bosch, F. C. 2003, *MNRAS*, 339, 1057, doi: [10.1046/j.1365-8711.2003.06254.x](https://doi.org/10.1046/j.1365-8711.2003.06254.x)
- . 2009, *ApJ*, 695, 900, doi: [10.1088/0004-637X/695/2/900](https://doi.org/10.1088/0004-637X/695/2/900)
- Yang, X., Mo, H. J., van den Bosch, F. C., & Jing, Y. P. 2005, *MNRAS*, 356, 1293, doi: [10.1111/j.1365-2966.2005.08560.x](https://doi.org/10.1111/j.1365-2966.2005.08560.x)
- Yang, X., Mo, H. J., van den Bosch, F. C., et al. 2007, *ApJ*, 671, 153, doi: [10.1086/522027](https://doi.org/10.1086/522027)
- York, D. G., Adelman, J., Anderson, John E., J., et al. 2000, *AJ*, 120, 1579, doi: [10.1086/301513](https://doi.org/10.1086/301513)
- Zandivarez, A., & Martínez, H. J. 2011, *MNRAS*, 415, 2553, doi: [10.1111/j.1365-2966.2011.18878.x](https://doi.org/10.1111/j.1365-2966.2011.18878.x)
- Zandivarez, A., Martínez, H. J., & Merchán, M. E. 2006, *ApJ*, 650, 137, doi: [10.1086/503894](https://doi.org/10.1086/503894)
- Zhang, W., Li, C., Kauffmann, G., & Xiao, T. 2013, *MNRAS*, 429, 2191, doi: [10.1093/mnras/sts490](https://doi.org/10.1093/mnras/sts490)
- Zhou, S., Mo, H. J., Li, C., Boquien, M., & Rossi, G. 2020, *MNRAS*, 497, 4753, doi: [10.1093/mnras/staa2337](https://doi.org/10.1093/mnras/staa2337)